M. Sc. Thesis

Physics

Ozone deposition over a boreal lake by the eddy covariance method

Pak Lun Fung

May 2018

Supervisor: prof. Timo Vesala and Dos. Ivan Mammarella

Reviewer: prof. Veli-Matti Kerminen and prof. Markku Kulmala

UNIVERSITY OF HELSINKI

Institute for Atmospheric and Earth System Research/ Physics

PL 64 (Gustaf Hällströmin katu 2)

00014 University of Helsinki

HELSINGIN YLIOPISTO — HELSINGFORS UNIVERSITET — UNIVERSITY OF HELSINKI

Tiedekunta/Osasto — Fakultet/Sektion — Faculty	Laitos — Institution — Department
Faculty of Science	Institute for Atmospheric and Earth System Research/ Physics

Tekijä — Författare — Author

Pak Lun Fung

Työn nimi — Arbetets titel — Title

Ozone deposition over a boreal lake by the eddy covariance method

Oppiaine —Läroämne — Subject

Atmospheric science

Työn laji — Arbetets art — Level	Aika — Datum — Date	Sivumäärä — Sidoantal — Number of pages
Master of Science	May 2018	60

Tiivistelmä — Referat — Abstract

Deposition is the main removal process of ground-level ozone. In some boreal areas, lakes accounts for up to 30% of the areas. However, there have been only few studies on ozone deposition over lake water in the past forty years. So far only one study has measured the ozone deposition velocity over lake (v_d) with the eddy covariance techniques. The 42-day campaign described in this thesis was held in August and September in 2012 in the Lake Kuivajärvi at SMEAR II station in Hyytiälä, Finland. The results showed a mean v_d of 0.88±0.05 mm s^{-1}, which was one-fifth of that over forest. v_d performed a weak diurnal cycle over lake which had a peak during the nighttime, while the forest showed the opposite. The lake data was classified into daytime and nighttime by a threshold of solar elevation angle (–2°). The two sets of data differed statistically by Mann-Whitney U test. A further analysis showed the higher v_d at night might be attributed to the more unstable atmospheric condition. Although, there is no evidence supporting a correlation of v_d with stability of the mixing layer in the lake, the dominance of mechanically-induced turbulence appeared to suppress v_d. By comparing with previous studies, elevated wind did not facilitate the rate of ozone deposition as expected.

Avainsanat — Nyckelord — Keywords

ozone deposition, deposition velocity, ozone flux, boreal, lake, eddy covariance, Kuivajärvi, Hyytiälä

Säilytyspaikka — Förvaringsställe — Where deposited

University of Helsinki

Muita tietoja — Övriga uppgifter — Additional information

Content

1. Introduction

The formation and depletion mechanism of tropospheric ozone (O_3) have been widely studied because of the recognized importance of its chemical and radiative properties in the atmosphere and the potential adverse effects it brings to the Earth. O_3 is the most important precursor of hydroxyl radical (•OH) in the troposphere (Atkinson and Aschmann, 1993). Both are fundamental to the high oxidizing power in the atmosphere. Since preindustrial times, the human-induced emissions of nitrogen oxides (NOx) and volatile organic compounds (VOCs), both being precursors of photochemical ozone production in the atmosphere, have been increasing and this led to a significant increase in the global concentration of tropospheric ozone (Atkinson and Aschmann, 1993). It has also been estimated that tropospheric ozone has at least doubled (Lamarque et al., 2005) and the rise continues (Oltmans et al., 1998; Vingarzan, 2004; Helmig et al., 2007). Tropospheric O_3 brings not only adverse effects to human's respiratory system (Simpson and Malik, 1996), but also a significant contribution (~15%) to anthropogenic greenhouse gas forcing (Luhar et al., 2017). Furthermore, a chronic exposure of high concentration of O_3 can lead to a loss of marketable crop yield and soil degradation (Krupa et al., 2001).

Based on simulations with global atmospheric chemistry models, dry deposition of ozone was estimated to create a global annual sink of 1094±264 Tg yr^{-1} (Luhar et al., 2017), which is more than double the tropospheric source of ozone through stratosphere-troposphere exchange of 477 ± 96 Tg yr^{-1} (Galbally and Roy, 1980; Young et al., 2013). This creates a strong motivation of studying the dependencies of ozone deposition process.

In the boreal zone, lakes are an important ecosystem, which cover 7% of the land area, while it has a global coverage of 3% (Downing et al., 2006). In some parts of Finland (Raatikainen and Kuusisto, 1990) and northern Canada (Spence et al., 2003), lake locally occupies up to 20% and 30% of the landscape, respectively. In Finland, the density of lakes is 56 lakes per 100km^2 on average (Raatikainen and Kuusisto, 1990) and the number of lakes with a surface area less than 0.01km^2 is over 130,000. Therefore, lake plays an indispensable role in determining atmospheric gaseous exchange process at local, regional and global scales (Krinner, 2003 and Samuelsson et al., 2010).

Eddy covariance (EC) technique is currently the most appropriate micrometeorological flux measurement method for the following reasons: (1) measurements represent a large footprint area;

(2) measurements are continuous with a high measurement frequency; (3) data collection is automatic and the equipment requires little maintenance. However, data post-processing and filtering EC data are demanding. There was a scarcity of long-term EC flux data over lakes (Nordbo et al., 2011), but, in recent years, the use of EC has grown its popularity in lake measurements (e.g. Eugster et al., 2011; Huotari et al., 2011; Podgrajsek et al., 2014; Heiskanen et al., 2014; Mammarella et al., 2015; Erkkilä et al., 2018).

However, in the current literature database, ozone deposition to lake water has only been mentioned by few studies, unlike that to forest (Zhou et al., 2017; Silva and Heald, 2018) and ocean (Ganzeveld et al., 2009; Luhar et al., 2017). To our understanding, there might be only one by Wesely et al. (1981) that showed the value of ozone deposition velocity over lake water using EC of 1 mm s^{-1}. A more recent review by Ganzeveld et al. (2009) reported deposition velocities ranging from 0.1 to 1 mm s^{-1} for freshwater or lake water and from 0.1 to 1.5 mm s^{-1} for ocean, involving other measurement techniques. Other studies show much higher values over land, ~4 mm s^{-1} (Hauglustaine et al., 1994), due to efficient uptake of ozone by the leaf stomata (Fan et al., 1990; Suni et al., 2003a) and high values of friction velocity in the daytime (Sun and Massman, 1999; Lamaud et al., 2002).

Deposition to surface is commonly described in atmospheric models by an analogy to electrical resistances (Liss, 1974; Wesely, 1989; Seinfeld and Pandis, 2016) and these resistances take physical, chemical and biological processes into account, depending on the surface type and species of interest. There have been several findings suggesting a relationship between the wind speed or friction velocity and ozone uptake over water surface (Galbally and Roy, 1980; Kawa and Pearson, 1989; Helmig et al., 2012; Heiskanen et al., 2014; Luhar et al., 2017). With increasing wind speed components, gaseous exchange at the water surface increases, especially under very high wind conditions (MacIntyre et al., 2001; Heiskanen et al., 2014; Podgrajsek et al., 2015). The mixing in the uppermost water column was also found to be associated with the deposition process in water due to the intensive stirring of the water (Ganzeveld et al., 2009). The constantly moving wave motion could lead to a significant increase in the rate of ozone uptake at the surface, and hence deposition velocity. The relative contribution of wind shear and buoyancy flux to turbulence at the air-water interface was also found to influence gaseous exchange processes in small lakes (Wanninkhof et al., 2009; Heiskanen et al., 2014).

Nevertheless, Ganzeveld et al. (2009) suggested that surface uptake rate was ~40 times faster than that expected from the ozone water solubility alone, inferring an enhancement through chemical

destruction (Schwartz, 1992). Physical processes, therefore, were suggested to hardly explain the full contribution to the deposition process. Apart from dissolved iodide, which was identified as a significant factor in ozone loss in the ocean at low wind speed (Garland et al., 1980; Chang et al., 2004), a laboratory study by Clifford et al. (2008) provided evidence for the role of dissolved organic compounds, including chlorophyll, in removal of ozone by water surfaces.

The main objective of this study was to analyze diurnal variations and possible driving forces of the lake O_3 deposition. Other objectives were to examine the environmental conditions for the whole period and to compare the O_3 deposition with the nearby forest. Unique measurements were carried out on the Julian day 233–274 in 2012 at Lake Kuivajärvi in Hyytiälä, Southern Finland. Basic meteorological data in the period was obtained as processed. Turbulence fluxes of O_3, measured by EC technique over the lake and the surrounding forest (SMEAR II), were used in the deposition velocity calculations. Diurnal variations of O_3 deposition in both lake and forest were analyzed and compared. Different averaging techniques and normalizations were also used to eliminate possible wind effects. To explore possible causes that give rise to the variability of deposition velocity, daytime and nighttime condition were defined in driving force analysis. Special focus was on the stability parameter, effective heat flux and waterside velocity scale ratio, which describes the extent of air and lake stratification.

In Section 2, detailed theory in variation and development of atmospheric boundary layer over different surfaces are explained, followed by the mechanism of lake stratification. The underlying theory of EC techniques and deposition process is also included. In Section 3, general site and measurement description are reported. Post-data processing and calculation procedures are also elaborated. In Section 4, I report and discuss the environmental conditions for the whole measurement period and compare the diurnal variation of O_3 deposition velocity in both lake and forest. A detailed driving force analysis is shown at the end of this section, as the highlight of the thesis.

2. Theory

2.1 Atmospheric boundary layer

The lowest atmosphere is a complex system. It includes a diurnal component (typically convection during the day and stratification in the nighttime over ground, vice versa over water body), complications due to complex terrain (surface elements such as buildings, forests, hills and mountains) and large weather events (replacement of air masses by prevailing winds, clouds and precipitation). Most of the turbulence, including all kinds of weather systems, takes place in the troposphere (below 10 km altitude), unlike the quiet stratosphere (10–50 km altitude), which is the layer immediately above.

Within the troposphere closest to the ground lies the Atmospheric Boundary Layer (ABL). It is less than 1 km thick at night and up to 2 km in extreme convective conditions. It is the layer where the atmosphere interacts with surface. This part of the troposphere is directly influenced by the presence of earth's surface and responds to surface forcing with a timescale of about an hour or less (Stull, 2012).

Sutton (1953) separated the boundary layer into two regions, as in Figure 1:

1. A surface layer region, or a constant flux layer, of 50–100 m deep of an approximately constant shearing stress and vertical turbulent fluxes with respect to height, where the flow is insensitive to the earth's rotation and the wind structure is determined primarily by surface friction and the vertical gradient of temperature.
2. An Ekman layer extends above the surface layer to a height of up to 2 km depending on the terrain type, where the shearing stress is variable, and the wind structure is influenced by surface friction, temperature gradient, and the earth's rotation (Kaimal and Finnigan, 1994).

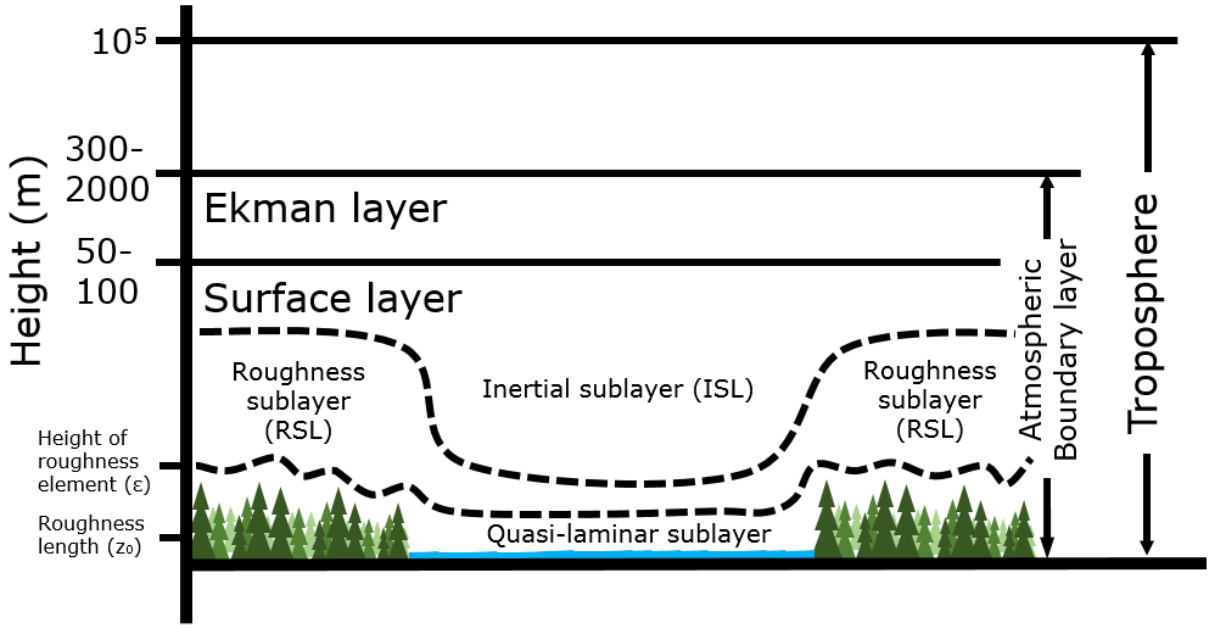

Figure 1. The schematic diagram to show the different layers in troposphere (not in scale).

2.1.1 Surface layer

The surface layer is further divided to an inertial sublayer (ISL) and roughness sublayer (RSL), which directly are influenced by individual roughness elements. Also, a quasi-laminar sublayer is always found immediately above the surface (Figure 1). Surface roughness elements have their own roughness lengths (z_0), proportional to the height of the roughness elements (ε), which affect the depth of different sublayers in the surface layer.

In general, when roughness elements are small, like lakes in our study ($z_0=10^{-3}$ *m*), the elements are submerged in ISL and it will be regarded as a smooth surface, even the flow in surface layer is always turbulent. On the contrary, if roughness elements are tall, for example, forest ($z_0=1$ *m*), the establishment of ISL will be prevented, and the flow is turbulent all the way down to the roughness elements. In this case, a rough surface is obtained. In both situations, a quasi-laminar sublayer is always formed right above every individual surface element, though the flow over the surface can be highly turbulent. The higher the flow velocity, the thinner the sublayer (McRae et al., 1982; Seinfeld and Pandis, 2016).

2.1.2 Diurnal behavior of atmospheric boundary layer

The diurnal behavior of ABL typically follows general patterns. To understand this behavior, we must consider the effects of buoyancy forces, which depend on atmospheric stability conditions (which, in turn, depend on the temperature profile). ABL plays an important role in maintaining or suppressing the energy of the turbulence. Therefore, we must consider the effect of non-adiabatic temperature profiles on the nature of turbulence in the surface layer. The way the atmospheric boundary layer is heated up or cooled down during day and night depends partly on changes in solar radiation. This behavior is also strongly reflected in the wind field.

Figure 2 shows a typical evolution of an atmospheric boundary layer over continent (Kaimal and Finnigan, 1994). During the night before sunrise, the surface layer is stable because the ground is colder than the air. A rising air parcel encounters warmer air around it and stops rising, which in turn causing a suppressed turbulence and the air flow is nearly laminar. This situation can be called surface inversion. In this stable boundary layer (SBL), turbulence decreases gradually with an increasing height, damped out by a combination of static stability and diminished wind shear.

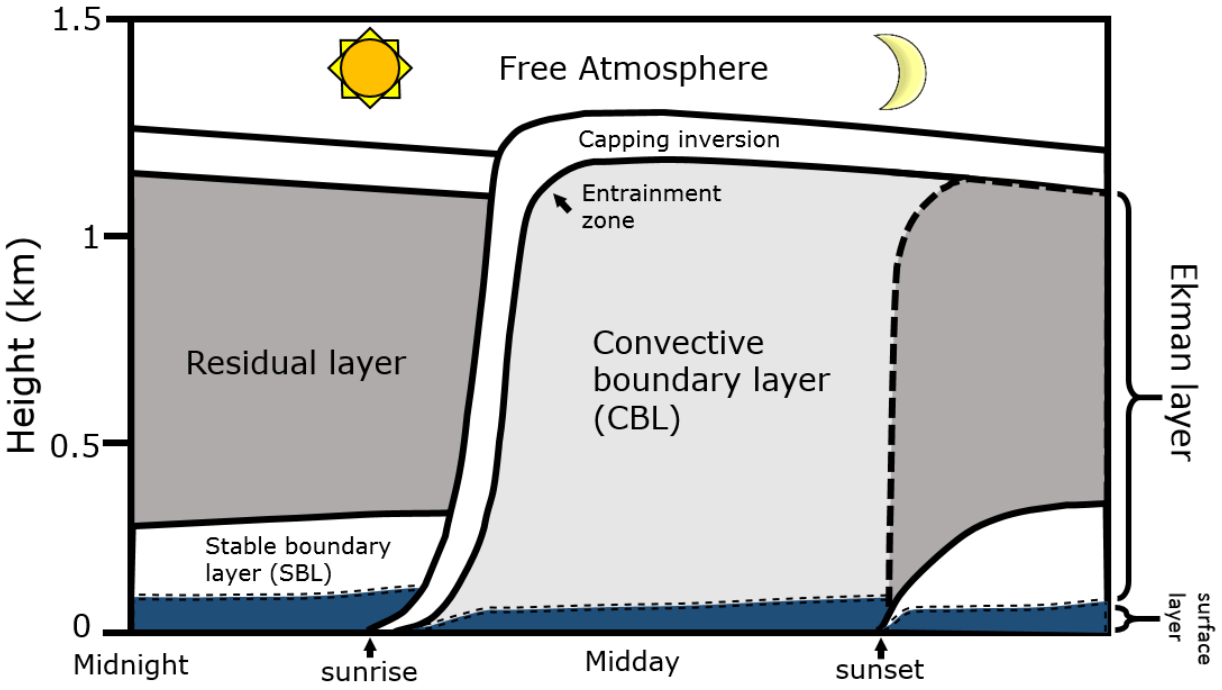

Figure 2. Diurnal evolution of the convective and stable boundary layers in response to surface heating and cooling over land (Kaimal and Finnigan, 1994).

As the sun rises on a clear sky day, a convective boundary layer (CBL) develops near the ground because solar radiation heats up the ground faster than the air (the light grey region in Figure 2). A warm rising air parcel encounters cooler air around it and continues rising, so that the near laminar flow of the nighttime stable air becomes turbulent. Throughout the day, as altitude increases, the effect of shear stresses at the surface in maintaining turbulence decreases and the effect of buoyancy increases. The warm thermals of air cause vigorous mixing aloft. The thickness of the layer of convective influence increases during the day, reaching heights of 1–2 km, as surface heating continues. The surface inversion that prevailed before sunrise evolves as the capping layer, as a lid damping out vertical motions, rising with convective layer as it grows upward. Often, the capping inversion will stay at about the same height through much of the afternoon. A strong morning inversion followed by subsidence through the day invariably produces a well-defined capping inversion. Within the CBL, convection is carried out by eddies that transport the heat all the way to the capping inversion base. There is also an entrainment process by which air from above the inversion base is drawn into the CBL in the regions of sinking motion (Figure 2).

In late afternoon with the approach of sunset, the thin air above the ground reaches the same temperature as the ground. Since there is no heat flux from the ground, the temperature profile becomes adiabatic. At this moment, the capping inversion weakens and there is a rapid collapse of turbulent motions in the CBL as the buoyancy forces that maintain them lose their energy source near the surface where the ground is cooling quickly from radiative heat loss to space. The convective layer is decaying and is transformed to residual layer (the dark grey region in Figure 2) in the absence of cold air advection. In the evening, the resulting heat flux to the ground causes a stable temperature profile close to the ground. The air immediately above the surface cools and mixes progressively upward through the action of turbulence generated by wind shear. The surface inversion that begins to form at the surface grows steadily to a thickness of 100–200 m by midnight. The wind speed is often very low at night, leading to a dominant stratification. Therefore, a shallow, stable surface layer can be discerned here as well, where the flow remains sensitive to the presence of the ground (Kaimal and Finnigan, 1994; Seinfeld and Pandis, 2016).

Over waterbody, the boundary layer depth varies relatively slowly in space and time. The water surface temperature changes little over a diurnal cycle because of the strong mixing within the top of the waterbody. Also, water has a large heat capacity, meaning that it can absorb large amount of heat

from the sun with relatively little temperature change. Thus, a slowly varying water surface temperature means a slowly varying forcing into the bottom of the boundary layer.

In summer season at high latitudes, the diurnal pattern of the boundary layer over waterbody is generally opposite to that over land. The water temperature is higher than in the air during the night, so a convective layer develops near the water surface. At sunrise, with the effect of solar radiation, the air above water surface is heated up faster than water is. The temperature profile becomes stable and the decaying convective layer will gradually be transformed into residual layer. At the same time, a surface layer is formed due to the collapse of turbulent flow and the enhancement of buoyancy forces, as its height becomes thicker as the daytime goes by. Approaching sunset, with the diminishment of radiation, air cools down faster than water does. It becomes unstable and convective, just like the way before sunrise (Kaimal and Finnigan, 1994; Seinfeld and Pandis, 2016).

2.1.3 Development of an internal boundary layer

The assumption of surface homogeneity can be a problem in practice. In our study, the lake has a relatively small size and is surrounded by a forest on land. The development of a boundary layer will not be the simple classical case anymore. When winds blow from forest to lake, it undergoes a change in surface roughness, which produces a change in surface momentum flux with a direct effect upon the wind field, and at the same time, an internal boundary layer (IBL) develops over the new surface, growing in height with downwind distance, fetch (Figure 3). It forms within the existing boundary layer, which is often called external boundary layer (Stull, 2012).

When air flows from a smooth surface to a rough surface, an airstream, traveling relatively rapidly over the smooth surface, generates a high stress on first encountering the roughness. As the new, rougher surface absorbs momentum from the air layers above it and this region of decelerated flow thickens into an internal boundary layer, the velocity of the air layer in contact with the enhanced roughness falls and so does the resulting surface stress. This results in horizontal convergence and upward motion above the boundary between smooth and rough.

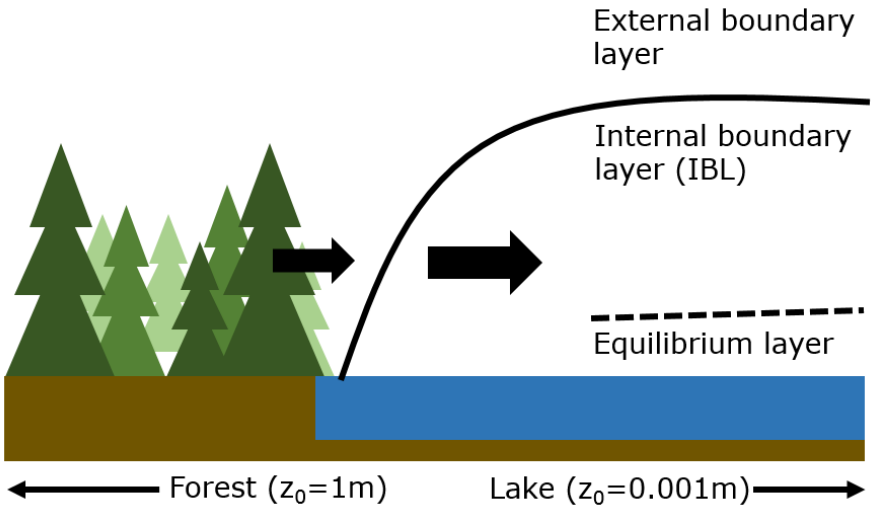

Figure 3. Schematic diagram of the formation of internal boundary layer from rough to smooth where z_o denotes roughness length (Stull, 2012).

On the contrary, flow from rough to smooth causes divergence and subsidence (Figure 3). The air layers arriving at the new surface are initially moving slowly and the stress drops as they encounter the smoother ground. They are then able to accelerate because the smooth surface absorbs less

momentum and the surface stress climbs until a new equilibrium is reached, where the adjustment of stress is slower than that from a smooth to a rough surface. The local equilibrium in turbulent kinetic energy forms the equilibrium layer only at an adequate fetch from the discontinuity of the roughness element, supported by wind tunnel experiments (Antonia and Luxton, 1972; Mulhearn and Finnigan, 1978). Concerning most of the small lakes surrounded by land, due to a small spatial extent (shorter fetch), an equilibrium is hardly reached with the local water surface (Aubinet et al., 2012). Back-calculation results reflect that large eddies with long timescales carry the memory of the upwind surface roughness, and hence the turbulent conditions do not quickly adapt to the smoother conditions of the lake surface as air travels from the rough surrounding terrestrial areas out to the lake surface (Jensen, 1978). However, Claussen (1991) suggested that the roughness can be felt at a small distance (300 z_0) upstream of the boundary, leading to a modification of wind profile mentioned above.

In either case, the flow field within IBL always displays characteristics of the new downwind surface. In external boundary layer, apart from the small perturbation caused by the pressure pulse at the change, the flow field is identical to the original flow.

Furthermore, upon a change in the temperature, for instance, when cold forest air advects over warmer lake (usually at night), a steady-state convective thermal internal boundary layer (TIBL) forms and deepens with fetch. It grows by entrainment, is suppressed by subsidence, like the classic CBL. Similarly, from warmer to cooler surface, usually during the day in our case, a stable TIBL forms. As the bottom of stable TIBL cools and approaches the surface temperature, the heat flux of the new surface becomes zero and the air stratifies, resembling the mechanism of SBL (see Section 2.1.2). Therefore, boundary layer conditions of the lake surrounded by forest can be changing all the time which leads to a complex phenomenon.

2.2 Lake stratification

Stratified lakes have a mixed layer (epilimnion) at the uppermost water column, followed by a stably stratified and denser water (hypolimnion) at the bottom (Figure 4). The two layers are separated by a transition layer, where a steep density gradient with depth is found. Since this density gradient is mostly a function of vertical temperature profile, the separation between the layers is called thermocline (Wetzel, 2001).

Epilimnion usually has the warmest condition in the summer due to solar radiation and it is prone to turbulent mixing due to wind. Hypolimnion is the coldest layer in the summer when the densest 4°C water sinks to the bottom. During summer, heat gain at the water surface stabilizes the water column. The external energy input is dissipated deeper in the lake, resulting in calmer and more stratified waters, thus lowering turbulent diffusivity. In this period, thermocline prevents the exchange between epilimnion and hypolimnion.

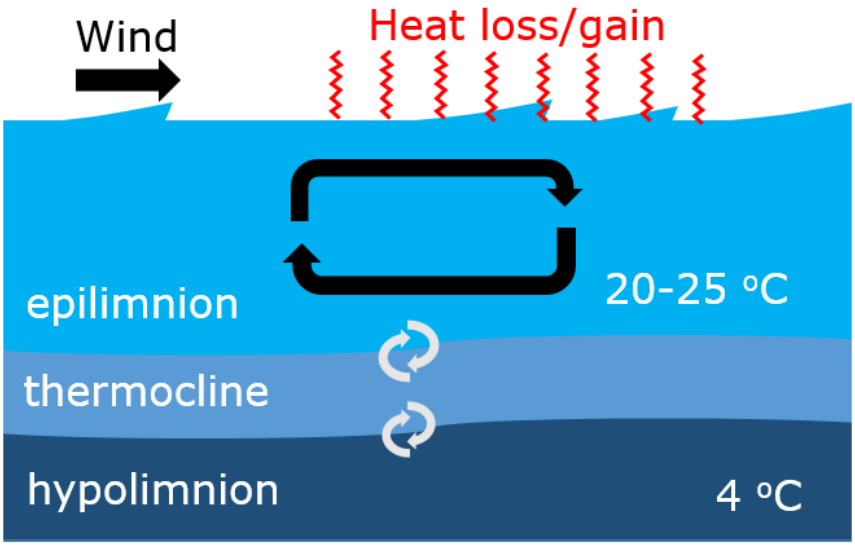

Figure 4. Schematic diagram to show typical lake stratification in the summer (Wetzel, 2001).

In the approach of the autumn, when the air is cooler than the lake, the surface water loses heat and becomes heavier than the underlying water masses. This causes convection in the mixed layer, and if the cooling is strong enough, these convective cells can reach the thermocline, causing turbulent mixing of the water and dissolved gases. Furthermore, when wind forcing is strong, it presses the surface masses to one end of the lake or the other and thermocline tilting takes place, resulting in breaking of internal waves (Monismith, 1985; Boegman et al., 2005).

When both convection and thermocline tilting occurs simultaneously, entrainment happens and increases the mixing of hypolimnetic water to the epilimnion. In this way, high concentrations of dissolved gases at the bottom can reach the surface (Crill et al., 1988; Eugster et al., 2003). As thermocline tilting intensifies, thermocline disappears eventually and the lake mixes throughout the whole water column. Mixing stops when the lake freezes and the lake stratifies again.

Similar mixing occurs also in the spring after the melting of ice. The just melted water is denser than the stratified water column, as a result of which convection, and hence overturn, starts. It stops when the densest water reaches the bottom and stratifies again in the summer. For boreal lakes, thermocline appears typically in the beginning of June and deepens through the summer until mixing starts in autumn.

2.3 Turbulent transport

Air motion is turbulent in the atmospheric surface layer. Turbulence is responsible for the transport of heat, water vapor, trace gases and aerosols in the atmosphere. Micrometeorology deals with the structure of the turbulent flow field and flow of atmospheric constituents between atmosphere and underlying surfaces. However, it is hard to define turbulence, but some characteristics of turbulent flows can be listed.

Turbulent flows are generally irregular and chaotic, which causes that the rates of momentum, mass and heat transfer may be many orders of magnitude greater than those due to pure molecular transport. Since turbulent velocities are randomly behaving variables, it is close to impossible to predict their exact values precisely. The determination of the statistical properties of the velocities and temperature can be useful and Reynolds decomposition is often used.

2.3.1 Reynolds decomposition

By Reynolds decomposition, each variable, ξ, in a timeseries can be decomposed into a time-mean part, $\bar{\xi}$, and a fluctuating part, ξ', where the averaging time, T, has to be larger than any of the time scales involved in the variations of ξ, as shown in Figure 5. This can be written as (Stull, 2012)

$$\xi(t) = \bar{\xi} + \xi'(t) \quad (1)$$

$$\bar{\xi} = \frac{1}{T}\int_{t}^{t+T} \xi(t)dt \quad , \quad (2)$$

There are few averaging rules upon the application of Reynold decomposition (Foken, 2008; Stull, 2012):

$$\bar{\xi'} = 0 \quad (3)$$

$$\overline{\xi\zeta} = \bar{\xi}\bar{\zeta} + \overline{\xi'\zeta'}$$

$$\overline{\bar{\xi}\bar{\zeta}} = \bar{\xi}\bar{\zeta}$$

$$\overline{a\bar{\xi}} = a\bar{\xi}$$

$$\overline{\xi + \zeta} = \bar{\xi} + \bar{\zeta} \quad .$$

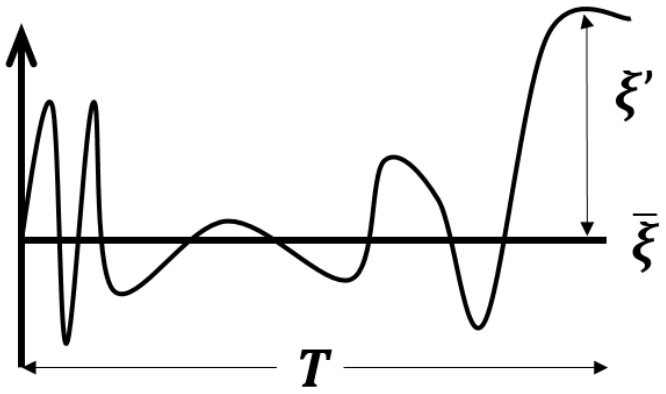

Figure 5. Schematic presentation of Reynolds decomposition in a timeseries, where T, $\bar{\xi}$ and ξ' denotes the averaging time, time-mean variable and fluctuating variable.

The mean variable could be determined, in principle, only by averaging the readings made over an infinite series of identical experiments, i.e. realizations under identical conditions (Kaimal and Finnigan, 1994). This averaging technique is called ensemble averaging and the time average equals to the ensemble average according to ergodic hypothesis (Brutsaert, 1982).

When we consider the time average of the fluctuating part, the fluctuations are equally distributed on either side of the average. The values describing the mean flow are smooth and slowly varying where the rapid variations are due to the fluctuations (i.e. eddies). It complies with the characteristics of turbulent flows, which includes extreme spatial and temporal variation. The turbulent fluctuations have considerably greater sizes than molecular scales. The largest fluctuations are comparable to the major dimensions of the flow, even the smallest eddies are still many orders of magnitude larger than molecular dimensions (order of 1 mm in the atmosphere). Thus, turbulence is responsible for most of the transport of momentum, mass and heat. The viscosity of the fluid prevents the fluctuations from becoming infinitely small (Aubinet et al., 2012).

2.3.2 Eddy covariance flux

A flux density describes how much of quantity moves through a unit area per unit time. A flux can be defined as an amount of a quantity that passes through a known surface per unit of time. The surface is called a source if net flux is away from the surface. While a net flux moves towards it, the surface is named a sink. For example, lake surface is a source of water released into the atmosphere

in the process of evaporation. Green canopy can be a sink of O_3 during the day as green leaves would absorb O_3 from the atmosphere through stomata (Burba and Anderson, 2007).

In a surface layer, air flow is turbulent, and it can be imagined as a horizontal flow of numerous rotating eddies, as in Figure 6. Each eddy has three speed components, including vertical movement of the air. Schematically, consider a point above the lake in our study, in a time frame, an eddy moves parcel downward through a cross section with the fluctuating vertical wind speed w'. Each parcel has its characteristics, such as concentration, temperature and humidity. At the same moment, it has a change in gas concentration, $\rho_c{}'$, and the net vertical flux over time could be calculated by taking covariance of two the instantaneous deviations.

Mathematically, under a turbulent flow, vertical flux, *Fc*, can be presented by a mean product:

$$F_c = \overline{\rho_a w s} \quad , \tag{4}$$

where ρ_a is air density, *w* is vertical wind speed and *s* is the mixing ratio of the gas.

Reynolds decomposition can be used to break the three variables into their means and deviations as in equation (4). The vertical wind speed will be presented as a mean over certain time, say 30 mins which has been a standard for terrestrial ecosystem studies (Nordbo et al., 2011; Mammarella et al., 2015), and an instantaneous deviation from this mean for every time unit (0.1 seconds in our study due to the sensor resolution). Similar procedures can be done with air density and mixing ratio of the gas by using equation (1):

$$F_c = \overline{(\overline{\rho_a} + \rho_a)(\overline{w} + w')(\overline{s} + s')} \quad . \tag{5}$$

The equation is further open by the techniques in equation (3):

$$F_c = \overline{(\overline{\rho_a}\overline{w}\overline{s} + \overline{\rho_a}\overline{w}s' + \overline{\rho_a}w'\overline{s} + \overline{\rho_a}w's' + \rho'_a\overline{w}\overline{s} + \rho'_a\overline{w}s' + \rho'_a w'\overline{s} + \rho'_a w's')} \quad . \tag{6}$$

The averaged deviation from the average are removed because averaged deviation from an average is zero. We obtain

$$F_c = \left(\overline{\rho_a}\overline{w}\overline{s} + \overline{\rho_a}\overline{w's'} + \overline{w}\overline{\rho'_a s'} + \overline{s}\overline{\rho'_a w'} + \overline{\rho'_a w's'}\right) \quad . \tag{7}$$

To simplify equation (7), we assumed the density fluctuations to be negligible. However, in case of

strong winds over a mountain ridge, density fluctuation $\rho_a{}'w'$ may be large, and should not be ignored. In our study, it can be safely assumed negligible as lake is flat. The equation becomes

$$F = \overline{\rho_a}\overline{w}\overline{s} + \overline{\rho_a}\overline{w's'} \quad . \tag{8}$$

From equation (8), the mean vertical flow is negligible for horizontal homogeneous terrain after taking coordination rotation, so that no flow diversions or conversions occur. In this case, the flux is defined as the product of the mean air density, and the mean covariance between instantaneous deviations in vertical wind speed and mixing ratio (Figure 6):

$$F_c = \overline{\rho_a}\overline{w's'} \quad . \tag{9}$$

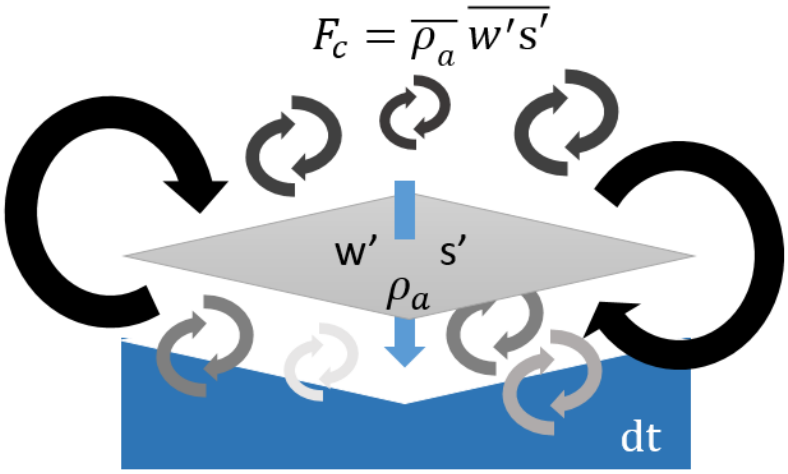

Figure 6. Schematic of how net eddy covariance flux is calculated at a point, where *Fc*, *w*, *s*, ρ_a and *dt* denote the vertical flux of the gas of interest, vertical wind speed, the mixing ratio of the gas and the detection time, respectively.

2.3.3 Stability parameter

The stability parameter (ξ) is the ratio of the measurement height z (m) to the Obukhov length L (m),

$$\xi = \frac{z}{L} \quad , \tag{10}$$

where L is proportional to the height above the surface at which buoyant factors first dominate over mechanical (shear) production of turbulence. For convective situations, buoyant and shear production terms are approximately equal at $z=-0.5L$. Typically, z has a positive value at night while a negative in the daytime.

L is defined as (Monin and Obukhov, 1954):

$$\mathrm{L} = \frac{-{u_*}^3 T_v}{kgQ_{v0}} \quad , \tag{11}$$

where k is von Kármán's constant, u_* (m s^{-1}) is the friction velocity (shown in Section 2.3.4.), Q_{v0} (K m s^{-1}) is a kinematic virtual temperature flux at the surface, T_v (K) is a reference virtual temperature, and g (m s^{-2}) is the gravitational acceleration.

The stability parameter is an important scaling variable for similarity hypothesis proposed by Monin and Obukhov (1954) of the surface layer. Although its magnitude is not directly related to static nor dynamic stability, its sign relates to static stability, negative when the atmosphere is unstable and positive when it is statically stable. A detailed classification of stability is shown in Table 1. This parameter is useful because L can be assumed constant through the surface layer.

Classification	Range
Extremely Unstable (EU)	z/L<–2
Very Unstable (VU)	–2<z/L<–0.6
Unstable (U)	–0.6<z/L<–0.2
Weakly Unstable (WU)	–0.2<z/L<–0.02
Near Neutral – Unstable (NN-U)	–0.02<z/L<0
Near Neutral – Stable (NN-S)	0<z/L<0.02
Weakly Stable (WS)	0.02<z/L<0.2
Stable (S)	0.2<z/L<0.6
Very Stable (VU)	0.6<z/L<2
Extremely Stable (ES)	z/L>2

Table 1. Classification of atmospheric stability (Sorbjan and Grachev, 2010)

2.3.4 Friction velocity

Friction velocity (u_*) is a reference wind velocity, which is usually applied to motion near the ground where the shearing stress is often assumed to be independent of height. It is a fundamental parameter in Monin-Obukhov similarity theory and is used to normalize velocities for cancelling effects of other vertical movement:

$$u_* = \sqrt{\frac{-\tau_0}{\rho_a}} = \sqrt[4]{(\overline{u'w'})^2 + (\overline{v'w'})^2} \quad , \tag{12}$$

where τ_0 (kg m^{-1}s^{-2}) is the total stress and ρ_a (kg m^{-3}) is the air density. It can be further represented by the covariance of the fluctuating parts of both vertical velocity and horizontal velocities (Sutton, 1953).

2.3.5 Waterside turbulent velocities

Both the waterside turbulent velocities, u_{*w} and w_{*w}, are estimated from the available atmospheric measurements. The waterside friction velocity is calculated as,

$$u_{*w} = u_{*a}\sqrt{\rho_a/\rho_w} \quad , \tag{13}$$

where u_{*a} (m s^{-1})is the friction velocity in the atmosphere, equivalent to u_*, and ρ_w (kg m^{-3}) is the water density (Deacon, 1977).

The waterside convective velocity w_{*w} is defined as,

$$w_{*w} = \sqrt[3]{-F_B * z_{ML}} \quad , \tag{14}$$

where F_B (m^2 s^{-3}) is the water side buoyancy flux (see equation (15)) and z_{ML} (m) is the actively mixing layer depth, which was estimated from the water temperature profile and calculated as the first depth where the temperature difference relative to the surface temperature at (0.2 m) was larger than 0.25°C.

The relative role of mechanically-induced (generated by wind) and buoyancy-induced (generated by convection) turbulence in the water can be studied with the ratio u_{*w}/w_{*w}. (Imberger, 1985) When mechanically induced turbulence dominates over buoyancy induced turbulence (u_{*w}/w_{*w} is high, >0.75), water-side turbulence will not penetrate as deeply as when the buoyancy is dominant (u_{*w}/w_{*w} is low, <0.75) (Imberger, 1985; MacIntyre et al., 2001).

2.3.6 Buoyancy flux and effective heat flux

The waterside buoyancy flux F_B ($m^2\ s^{-3}$) can be used as a measure of convection:

$$F_B = \frac{g\alpha Q_{eff}}{c_{pw}\rho_w} \quad , \tag{15}$$

where a is the thermal expansion coefficient, Q_{eff} (W m^{-2}) is the effective surface heat flux and c_{pw} (J K^{-1}) is the specific heat of water. Q_{eff} is the sum of latent and sensible heat flux, net longwave radiation and the portion of shortwave radiation within the actively mixing layer (Imberger, 1985):

$$Q_{eff} = Q_{Snet} + Q_{SW}(0) + Q_{SW}(z_{ML}) - \frac{2}{z_{ML}}\int_{z_{ML}}^{0} Q_{SW}(z)dz \tag{16}$$

$$Q_{Snet} = Q_{LWnet} - H - LE \quad , \tag{17}$$

where Q_{Snet} is the net heat flux, Q_{LWnet} is the net longwave radiation, and Q_{SW} is the shortwave radiation. As an approximation, shortwave radiation is assumed to contribute to the surface buoyancy flux except the part penetrating into the water column in the mixing layer. The penetration of solar radiation into the water column was parameterized by the Beer-Lambert's law as indicated by the integration from lake surface (0 m) to the depth of the actively mixing layer (z_{ML}). A constant value of 0.59 was used for the diffuse light extinction coefficient as estimated by Heiskanen et al. (2015) for Lake Kuivajärvi. The effective heat flux represents the actual heating of the actively mixing layer. When the effective heat flux is greater than zero, the uppermost part of the water column will stratify and be more stable. When it is less than zero, cooling takes place and turbulence can be induced not only by shear but also by heat loss (convective mixing). In the nighttime, in the absence of solar radiation, the effective heat flux equals the net surface heat flux. (Podgrajsek et al., 2014; Mammarella et al., 2015)

2.4 Deposition process

In this study, we mainly focus on the dry deposition process by which ozone gas is removed from the atmosphere. In general terms, dry deposition is the transport of gaseous species from the atmosphere onto surfaces in the absence of precipitation. To describe the dry deposition from the bulk atmosphere to water body, deposition velocity, v_d (mm s^{-1}), is often used, regarded as a flux normalized by the difference in concentration:

$$v_d = \frac{-F_c}{\Delta C} \quad , \tag{18}$$

where F_c (derived from equation (9)) represents the vertical dry deposition flux and ΔC is the concentration difference between heights at the measurement platform and the deposition interface. By convention, a downward flux is negative, so that v_d is positive for a depositing substance, and vice versa. This parameterization has been widely used in literature since it represents all the complexities of the deposition process (Seinfeld and Pandis, 2016).

By using an electrical resistance analogy, the transport of material to the surface is assumed to be governed by three resistances in series (Figure 7): the aerodynamic resistance (r_a), the quasi-laminar resistance (r_b), and the surface resistance (r_c), corresponding to the three steps of deposition. The total resistance of the gas deposition (r_T) is the sum of the three individual resistances. For gases at steady-state, overall flux can be related to the concentration differences and resistances across the layers (Seinfeld and Pandis, 2016):

$$F_c = \frac{C_3 - C_2}{r_a} = \frac{C_2 - C_1}{r_b} = \frac{C_1 - C_0}{r_c} = \frac{C_3 - C_0}{r_T} \quad . \tag{19}$$

As C_o in the liquid phase is assumed to be zero, combining equation (18) and (19), v_d is the inverse of the total deposition (Liss, 1974; Wesely and Hicks, 2000):

$$v_d = \frac{1}{r_T} = \frac{1}{r_a + r_b + r_c} \quad . \tag{20}$$

The aerodynamic component, r_a, generally represents the aerodynamic transport down through the atmospheric surface layer to a very thin stagnant layer (0.1–1 mm) of air in direct contact with the surface and not moving with the mean flow of the wind, usually called the quasi-laminar sublayer. The magnitude of r_a is typically based on gradient transport theory and mass transfer/ momentum transfer similarity, which is not further described here. The quasi-laminar resistance, r_b, denotes the

molecular transport across this thin quasi-laminar sublayer, to the surface itself, regardless of the orientation of the target surface. It depends on the molecular diffusivity of the gas and is relatively insensitive to roughness length z_0 (Seinfeld and Pandis, 2016). However, according to Jacob (1999), r_b tends to be very small compared to r_a, so the specification of r_b is of little importance. The surface resistance, r_c, for gases depends critically on the nature of the surface. Solubility and chemical reactivity may also affect the uptake at the surface.

In a water body, the transfer of ozone from the gas phase to a liquid phase can be illustrated in Figure 7. The gas phase is assumed to be well mixed by turbulence down to a thin stagnant film just above the air-lake interface. Likewise, it is assumed that all the resistance to mass transfer of the dissolved ozone away from the interface into the bulk liquid is confined to a thin stagnant layer of liquid just below the air-water interface. Right at the interface, the partial pressure of ozone in the gas phase is in equilibrium with the concentration of ozone in the liquid phase. This traditional representation of mass transfer between two phases is called the two-film model. The gas-phase flux of ozone across the thin film to the interface is represented in terms of a gas-phase mass transfer coefficient K_{G,O_3}. At a steady state, this flux must be equal to that of dissolved ozone away from the interface into the bulk liquid phase and this flux is written in terms of a liquid-phase mass transfer coefficient K_{L,O_3} (Seinfeld and Pandis, 2016):

$$F_c = K_{G,O_3}\left(P_{O_3G} - P*_{O_3}\right) = K_{L,O_3}\left(C*_{O_3} - C_{O_3L}\right) \quad , \qquad (21)$$

where $P*_{O_3}$ is the gas-phase partial pressure that would be in equilibrium with the bulk liquid-phase concentration C_{O_3L} while $C*_{O_3}$ is the liquid-phase concentration that would be in equilibrium with the bulk gas-phase partial pressure P_{O_3G} for ozone. After undergoing the thin stagnant layer below the interface, ozone is further mixed by the convection in the lake. Wanninkhof et al. (2009) reported that environmental factors, like wind speed, affect the partial pressure and diffusive flux over the air-water interface, especially during low wind conditions (Rutgersson et al., 2011).

Since ozone is a slightly soluble gas, r_c is controlled not only by the two mass transfer coefficients, but also the effective Henry's law constant $\widetilde{H_{O_3}}$ of ozone as (Seinfeld and Pandis, 2016):

$$r_c = \frac{1}{K_{G,O_3}} + \frac{1}{K_{L,O_3}\widetilde{H_{O_3}}} \quad . \qquad (22)$$

By equation (20), dry deposition tends to be controlled by the surface resistance, r_c. For ozone deposition, it exhibits both air-side and waterside resistance, consequently leads to a large r_c, and

hence a smaller v_d. If chemical reactions are involved in the ozone deposition process, the liquid-phase mass transfer coefficient K_{L,O_3} is no longer influenced simply by diffusivity, as a significant poriton of the ozone dissolved in the liquid phase is depleted continuously. Due to its low solubility and its high reactivity, the reaction is usually fast. It takes place only at the surface and no ozone is transferred into the bulk of the liquid phase. Therefore, it has a relatively small penetrating depth, which is of the order of a few μm (Fairall et al., 2007). In other cases when the chemical reaction is slow, the direct effect of reacting dissolved compounds on the ozone deposition can be neglected. This enhancement depends on the relative concentration of ozone and its reactants in each phase, its solubility, and the relative resistance of the mass transfer and reaction steps (Contreras Iglesias, 2003). However, the details of the ozone chemical enhancement with water is beyond the focus of this thesis.

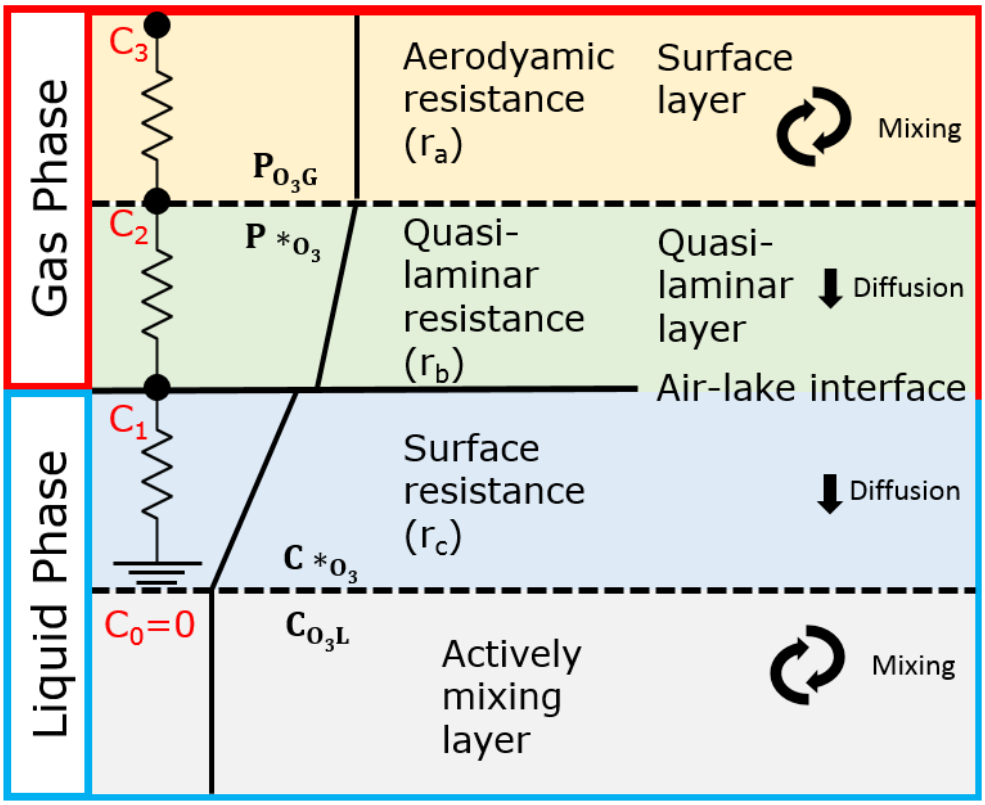

Figure 7. Schematic of resistance analog and two-film model for ozone deposition over lake water (not in scale).

3. Materials and methods

3.1 Site description

3.1.1 The Lake Kuivajärvi

The flux campaign was conducted at Lake Kuivajärvi (61^{o} 50'N, 24^{o} 17'E), located in the vicinity of the Hyytiälä Forestry Field Station and SMEAR II Station (Hari and Kulmala, 2005), for 43 days in August and September in 2012 (data of a period of 23 days after data processing, see Section 3.3.2). Lake Kuivajärvi is a small humic boreal lake extending about 2.6 km along northwest to southeast direction with a width of few hundred meters and a maximum depth of 13.2 m, which is deeper than most lakes in Finland. Its surface area is 0.63 km^2.

Lake Kuivajärvi is mainly surrounded by a managed coniferous forest, but also, small open wetland areas, mainly in southwest and west. Except the surroundings around the outlet in the southern end of the lake, the littoral zone fringing the lake is small and sparsely vegetated.

The measurement platform was situated approximately 1.8 km and 0.8 km from the northern end and southern end, respectively. The depth at the location of the platform is 12.5 m. The moored platform, firmly anchored from all the four corners, has a size of about 3.1 x 6.2 m, which is appropriate size for being stable and, on the other hand, minimizing distortion effects on the turbulence measurements (Mammarella et al., 2015).

3.1.2 The surrounding forest

The forest data was taken in a 128-meter-high tower at SMEAR II Station in Hyytiälä, located close to Lake Kuivajärvi. The coniferous forest is relatively homogeneous around the tower for about 200 m to all directions, extending about 1 km to the North. It is dominated by Scots pine stand, established in 1962, and the rest is covered by Norway Spruces and deciduous trees (Bäck et al., 2012). The dominant tree height from 2000 to 2010 was about 14–18 m. The understory vegetation mainly consists of lingonberry and bilberry with a mean height of 0.2–0.3 m. The forest floor is covered by dense mosses. Underneath is a 5cm layer of humus in soil (Kolari et al., 2006; Kulmala et al., 2008).

3.2 Measurements

3.2.1 Eddy covariance measurements

Turbulence fluxes of latent heat, sensible heat and O_3 were measured using the EC technique. The system, located on the abovementioned lake platform, includes an ultrasonic anemometer (Metek USA-1, GmbH, Elmshorn, Germany) to measure the three wind velocity components and sonic temperature and a fast chemiluminescent gas analyzer FOS (Sextant Technology Ltd, New Zealand) that measures O_3 concentration. A closed-path infrared gas analyzer (LI-COR Inc., Lincoln, NE, USA) was used to measure H_2O concentration fluctuations for the calculation of latent heat fluxes. The data was sampled at 10Hz, and the gas inlet was at 1.7 m above the water surface close to the sonic anemometer (horizontal and vertical separation were about 3 and 12 cm, respectively). The polytetrafluoroethylene (PTFE) sampling line was 0.7 m long, and the inside diameter was 4 mm. The flow rate inside the sampling line was 12 L min^{-1}. Fast measurements of the platform tilt angles were performed using a dual-axis inclinometer (SCA121T-D01, VTI Technologies Oy, Vantaa, Finland, now Murata Electronics Oy), in order to assess the platform oscillation caused by waves (Mammarella et al., 2015).

For tower measurement, the observed quantities include O_3 concentration (TEI 49C ultraviolet light absorption analyser) at 16.8 m and 33.6 m and O_3 flux (Gill Solent HS 1199 sonic anemometer and Unisearch Associates LOZ-3 gas analyzer) at 23 m. The measurement data at SMEAR II were obtained through AVAA open data publishing platform (http://avaa.tdata.fi/web/smart/smear), which was introduced originally by Junninen et al. (2009).

3.2.2 Ancillary measurements

Continuous measurements of the water temperature were carried out by a chain of Pt-100 temperature sensors installed at the depths of 0.2 m, 0.5 m, 1.0 m, 2.0 m, 2.5 m, 3.0 m, 3.5 m, 4.0 m, 4.5 m, 5.0 m, 6.0 m, 8.0 m, 10.0 m and 12.0 m. The sampling frequency was 0.2Hz, and the probe resolution and accuracy were 0.1 and $\pm$0.5°C, respectively. The shortwave and longwave radiation of components were measured with a CNR-1 net radiometer (Kipp & Zonen B.V., Delft, Netherland), mounted at 1 m above the water surface on a horizontal boom extending 1.2m from the platform. Air temperature and ambient relative humidity were measured by the Rotronic MP106A sensor (Rotronic

AG, Bassersdorf, Switzerland) installed inside a naturally ventilated radiation shield at 1.5 m height. All ancillary measurements were averaged to half-hour resolution (Mammarella et al., 2015).

3.3 Data processing

3.3.1 Raw data post-processing

All measured fluxes, including heat fluxes and O_3 fluxes from lake platform and tower, were calculated as half hour block-averaged covariance between the scalars and the vertical wind velocity using EddyUH software (Mammarella et al., 2016) based on standard methodology (see Rannik et al., 2012). The O_3 concentration was also 30-min averaged to fit consistently with the EC flux resolution. The tower ozone concentration was linearly interpolated using the data collected at 16.8 m and 33.6 m to obtain the estimated parameter values at 23 m for a direct calculation of deposition velocities.

Spikes were removed in the first data processing stage. Kurtosis and skewness of the data distribution were also assessed that data other than $1< |Ku| <8$ and $-2< |Sk| <2$ were discarded to improve data quality (Vickers and Mahrt, 1997). No gap-filling was attempted.

The data from the 42-day project was reduced to a period of 23 days from day 235 to 257. Within this period, data on day 239 were even totally eliminated. A large portion of data at midnights on day 237, 240 and 244 were also missing, which made the distribution of data uneven throughout the day.

3.3.2 Possible inappropriate conditions

Wind directions other than along the lake ($130^o <wd <180^o$ and $300^o <wd <330^o$) were ignored to avoid fluxes coming from the forest (Mammarella et al., 2015) due to footprint distribution along the lake as the main reason. When wind blows from the forest, it undergoes an establishment of internal boundary layer. The measurement at the lake does not completely represent itself (see Section 2.1.3). A minor reason is the advection of O_3 from the forest as Rannik et al. (2009) suggested it causes scatters in lake flux measurement, especially at night under strongly stable conditions, but, in a less affected way compared to CO_2. In addition, Eugster et al. (2003) and Vesala et al. (2006) proposed that the advection effect can also be removed by changing the averaging period of the flux, from

30 min to 5 min. This procedure disregards low frequency contribution in the flux estimation. However, this change of averaging period is beyond the focus of the study, so no modification was attempted. Data under low turbulence condition were once considered to be omitted due to the possibility of lower accuracy of eddy covariance technique. This procedure was questioned by Aubinet et al. (2012) for lake environment. In addition, no clear friction velocity (u^*) threshold cannot be determined by simple plotting deposition velocity against binned average u^*, as a result, no such filtering was applied.

Eventually, in the period of 23 days, 48% of the data were omitted due to raw data post-processing, as well as some further 8% because of inappropriate wind direction, which added up to 56% in total. The omission rate is similar for both daytime and nighttime condition, 55% and 58%, respectively. However, the fraction of the rejected data is relatively high for daytime condition, as the normal rejection case is 20–30% and 50–60% of daytime and nighttime eddy covariance data, respectively (Suni et al., 2003b). The 80% flux footprint reaches 100–300 m from the lake platform, determined by the atmospheric stability and wind direction (Mammarella et al., 2015).

3.3.3 Normalization of deposition velocity

Since the deposition process is believed to have a strong dependency on wind, in order to truly analyze the correlation of deposition velocity with other parameters, it might be useful to normalize deposition velocity by the other two velocity quantities, u^*_w and wind speed (U). The effect acting by the two quantities would be removed and a more explicit pattern might be found. The assessment of this normalization was shown in driving force analysis in Section 4.4.

3.3.4 Classification of conditions

Since the gaseous exchange process over lake is believed to vary diurnally (Podgrajsek et al., 2015; Erkkilä et al., 2018) due to the variation of atmospheric boundary layer and the mixing of surface water, so the O_3 deposition process can also be assumed to have such similar property. The data were therefore separated into two conditions, based on the solar elevation angle (Mammarella et al., 2015; Zhou et al., 2017): daytime and nighttime. The data points were considered as daytime condition when the solar elevation angle is greater than –2° and as nighttime condition when the solar elevation angle was smaller than or equal to –2°. Relative humidity was also once considered as a factor of

classification as in some other studies (Rannik et al., 2012; Zhou et al., 2017). However, the relative humidity was mostly high (above 70%) during the measurement period. Since there were insufficient data for dry condition, so it is not included in this study.

To illustrate that the two groups of datasets have different distributions, the Mann-Whitney U test was used (Erkkilä et al., 2018). For extensive data points more than 20, all the observations in sample 1 were each assigned a numeric rank in ascending order. The observed ranks were then summed up as T_1. U_1 and Z_1 and was given by (Lowry, 2014):

$$U_1 = n_1 n_2 + \frac{n_1(n_1+1)}{2} - T_1 \quad , \tag{23}$$

$$Z_1 = \frac{U_1 - (\frac{n_1 n_2}{2})}{\sigma_{U_1}} \quad . \tag{24}$$

where σ_{U_1} is the standard deviation of U_1. Similar calculation can be done for another sample. By comparing the obtained Z value with the critical Z value, whether the two samples are statistically significant can be determined. The significance level was set at 95%, implying that, for p-values lower than 0.05, the null hypothesis of 'two groups differing significantly' is considered to be true (Lowry, 2014).

4. Results and Discussion

4.1 Environmental conditions and water column temperature

In the first half of the measurement period, the daily pattern of air temperature was stable, with a cycle of slightly above 15 °C in the daytime and around 10°C in the nighttime (Figure 8a). On day 250–254, an air temperature drop episode was recognized and the lowest temperature (2.4 °C) was recorded on day 254. On the last two days of the campaign, the temperature rose back to normal and reached the peak of 18.9 °C on day 255. The variation of surface water temperature was comparably steady and generally higher than the ambient temperature. A gradual decline was identified with the lowest temperature of 13.2 °C at the end of the project.

The sensible heat flux (*H*) was mostly positive (Figure 8d), indicating the direction from the lake to the atmosphere, which was reasonable in the fall when surface water is warmer than the air. However, on day 255, about half of the day had a record of negative H. This is due to the exceptional condition of the air temperature exceeding the surface water temperature.

The latent heat flux (*LE*) was also generally positive (Figure 8d), but had a slightly larger magnitude than *H*, except at some midnights at the end of the campaign. In the second half of the measurement period with continuous data, a diurnal cycle of the latent heat flux was observed, with daytime peaks when most of the solar radiation reached the water body for evaporation, because of the smaller temperature difference between air and the lake water.

The wind speed (*U*) was stronger, up to 5.2 m s^{-1}, in the daytime than in the nighttime (Figure 8b). An exception to this pattern was found on day 249 with an intensifying wind during the night, which reached its highest at midnight. One remarkable finding was that, during the air temperature drop episode (see above), the wind direction was mostly from the North, but once the air temperature increased back to normal at the midnight on day 254, it blew from the South again. This could be explained by a cold front from the North on that occasion. The wind direction in the whole period was mainly from the South (130°–180°) and the North (300°–330°), along Lake Kuivajärvi, independent of the time of the day (Figure 8c and Figure 9). There were also periods when the wind rotated, for example, on days 237–238, 242, 247–248 and 250–252.

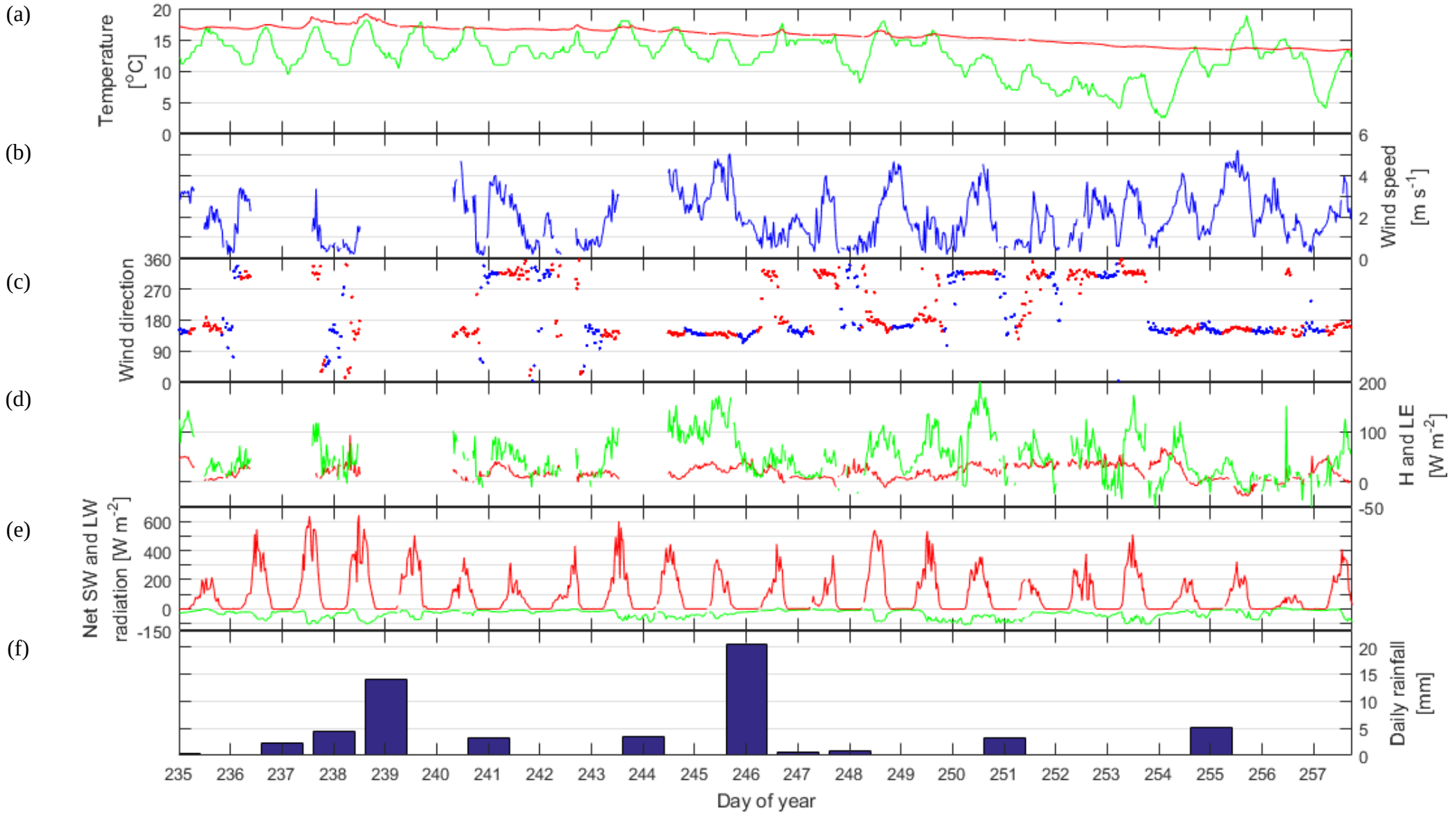

Figure 8. (a) The measured surface water temperature (° C, red line) and air temperature (green), (b) the wind speed (m s^{-1}) (c) the wind direction of day (blue) and night (red), (d) the sensible (red) and latent (green) heat flux (Wm^{-2}), (e) the net shortwave (red) and longwave (green) radiation (Wm^{-2}), and (f) the daily rainfall (mm). The x-axis is Julian day in the year for all the graphs and the values are half-hour averages except (f). Dateticks represent midnight except (f).

During the entire period, only four days were recorded with daily precipitation greater than 5 mm. The rainfall intensity on day 246 even exceeded 20 mm (Figure 8f). Net shortwave radiation and longwave radiation are presented in Figure 8e, where daily cycles were recognized. The amplitude of the former variable revealed the cloudiness of the day, whilst the width of the daily cycle approximated sunrise and sunset times. The positive net shortwave radiation indicated an absorption of radiant energy from the sun to the lake. The negative net longwave radiation, on the other hand, implied that energy was emitted from the lake when it obtained a sufficiently hot water surface. As a result, the peaks of both variables were found at midday when maximum solar energy reached the ground.

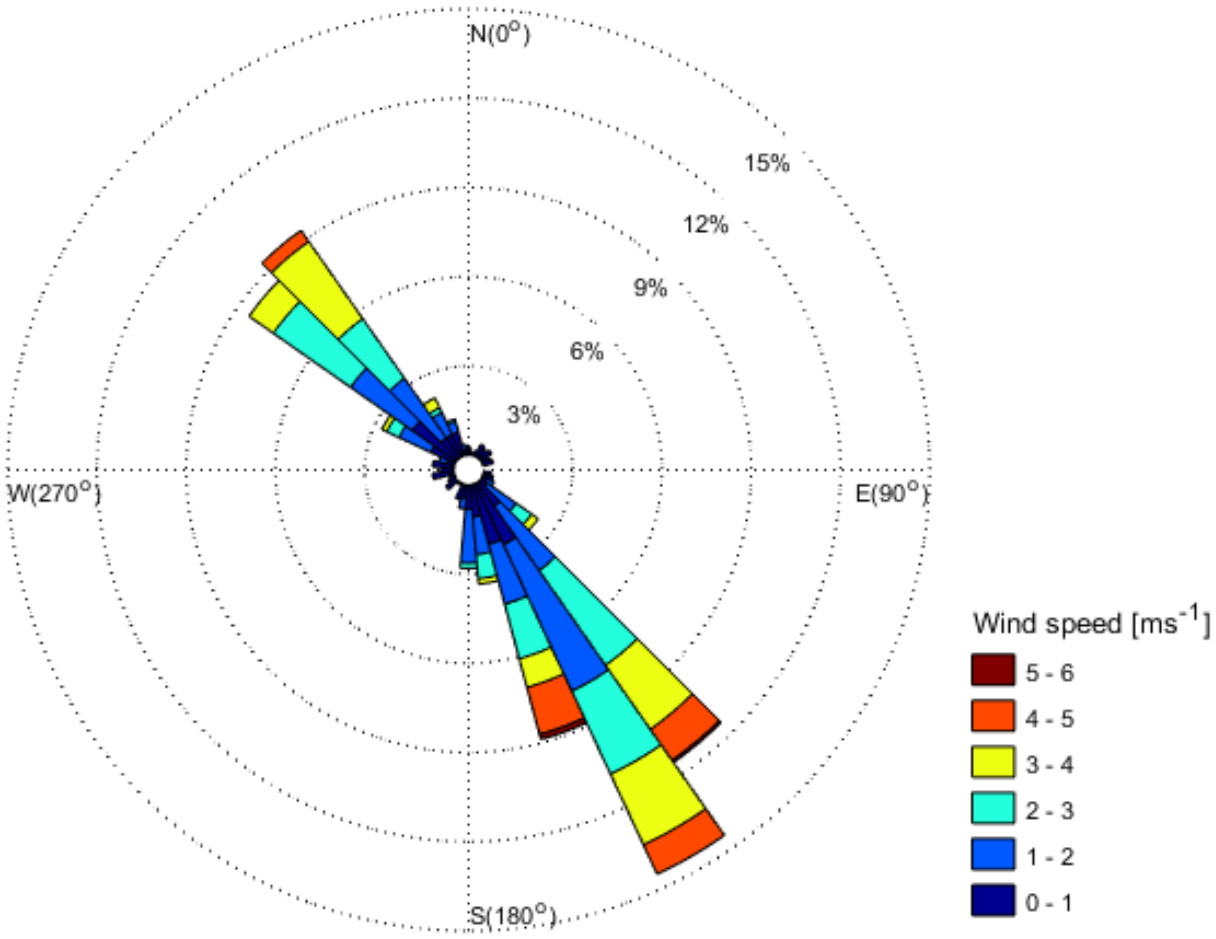

Figure 9. Wind rose of Lake Kuivajärvi shows wind direction and wind speed according to the frequency of occurrence (presented in percentage) during the measurement period.

The water column was thermally stratified during the whole campaign with a progressive thickening of the actively mixing layer, from about 3 m in the beginning to around 6 m at the end of the project, as demonstrated by the calculated depth of actively mixing layer, z_{ML} (see Secton 2.3.5) (Figure 10). The drop in temperature with north winds on days 250–255 even triggered a more intensifying mixing

in the water column. Although the mixing occurred at a deeper level, there was still a clear thermocline, which separated the actively mixing layer from the bottom of the lake. The measurement period was short and there is no clear definition of when overturning process starts, though it usually happens in late September in Kuivajärvi. Yet, it is evident that actively mixing layer was deepening, and accordingly, the measurement period might be the transition period from stratification to overturn.

While most of the data of waterside friction velocity ($u*_w$) fell within 0.01 m s^{-1} range, occasional booms, up to 0.018 m s^{-1}, were found in the second half of the measurement period (Figure 11a). At the same time, a vague daily pattern for the $u*_w$ could still be found despite the numerous spikes on the curve. It also appeared to be consistent in the first half of the measurement period, but from day 248 onwards, the daily maximum value dropped every day.

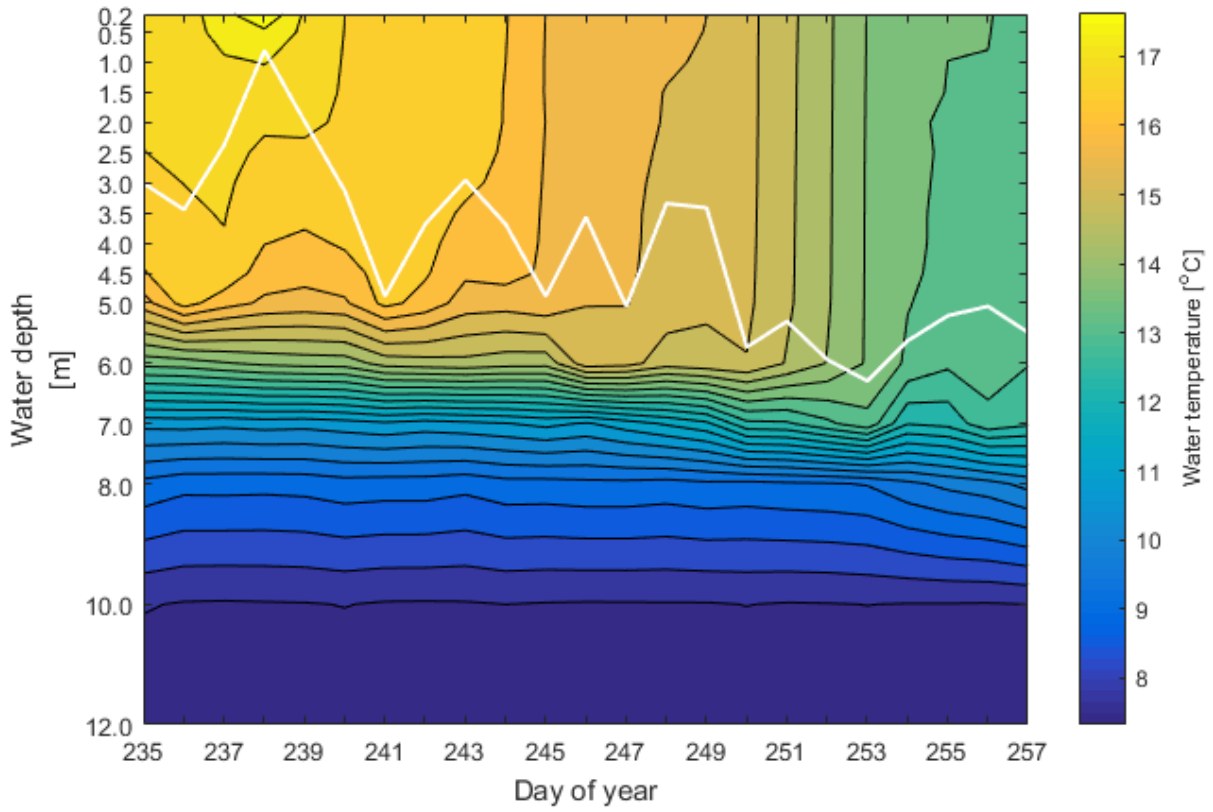

Figure 10. Daily averaged temperature profile in the water column in Lake Kuivajärvi. The white solid line represents the calculated depth of actively mixing layer, z_{ML}.

In most of the time, the stability parameter, z/L, showed a negative value, typically between −2 (unstable condition) and −0.01 (near-neutral condition), implying overall unstable atmospheric condition (Figure 11b and Table 1 on p.19). In such conditions, the atmosphere over the lake was seemingly more unstable in the nighttime than in the daytime owing to the bigger temperature difference between the air and the water. However, apart from infrequent, scattered positive data points, a set of patterned positive data was found on days 254–256. Starting from midnight, the atmospheric condition was getting less unstable then the sunrise approaches. At a certain time after midday, the atmosphere became stable and gained stronger stability throughout the day until the midnight on the following day. This pattern repeated over the three days. The reason might be that the air was continuously warmer than the surface water on day 255. The air over the air-water interface lost heat from the surface, therefore the air in the atmosphere tended to stratify and became more stable during the day (Heiskanen et al., 2014).

The effective heat flux is shown in Figure 11c. The data ranged from –225 W m^{-2} to 210 W m^{-2} for the whole period, with more than half of the data on the negative side. This depicted cooling took place in the uppermost water column, which resulted in an overall convective mixing (consistent with the water temperature profile). It had records of positive values in occasional middays, which showed actual heating, and in turn stabilization, to the actively mixing layer. This is reasonable as the solar energy was the strongest in middays and the portion of surface heat flux contributing heating to the uppermost water column was also the greatest in normal case. In general, effective heat flux in the daytime were higher than in the nighttime.

In order to determine the conditions when the buoyancy flux makes a considerable contribution to mixing relative to wind in the actively mixing layer, the ratio of the two waterside velocities was shown in a logarithm scale in Figure 11d. The figure showed an overall domination of wind forcing in waterside convective mixing (ratio>0.75), which is in alignment with Read et al. (2012) and Podgrajsek (2015).The distribution of waterside velocity scale ratio tended to have values greater than 0.75 during the day and less than 0.75 at night. The former case represented a domination of mechanically-induced turbulence over buoyancy-induced turbulence due to the general higher air temperature and stronger wind in the daytime (Imberger, 1985). Nighttime condition was usually calm, with lower wind speeds and no solar radiation, so the buoyancy outweighed the influence by wind shear. However, the data on day 248 and 249 showed an irregularity. All the numbers illustrated a domination of mechanically-induced turbulence for the entire two days, although the pattern was similar.

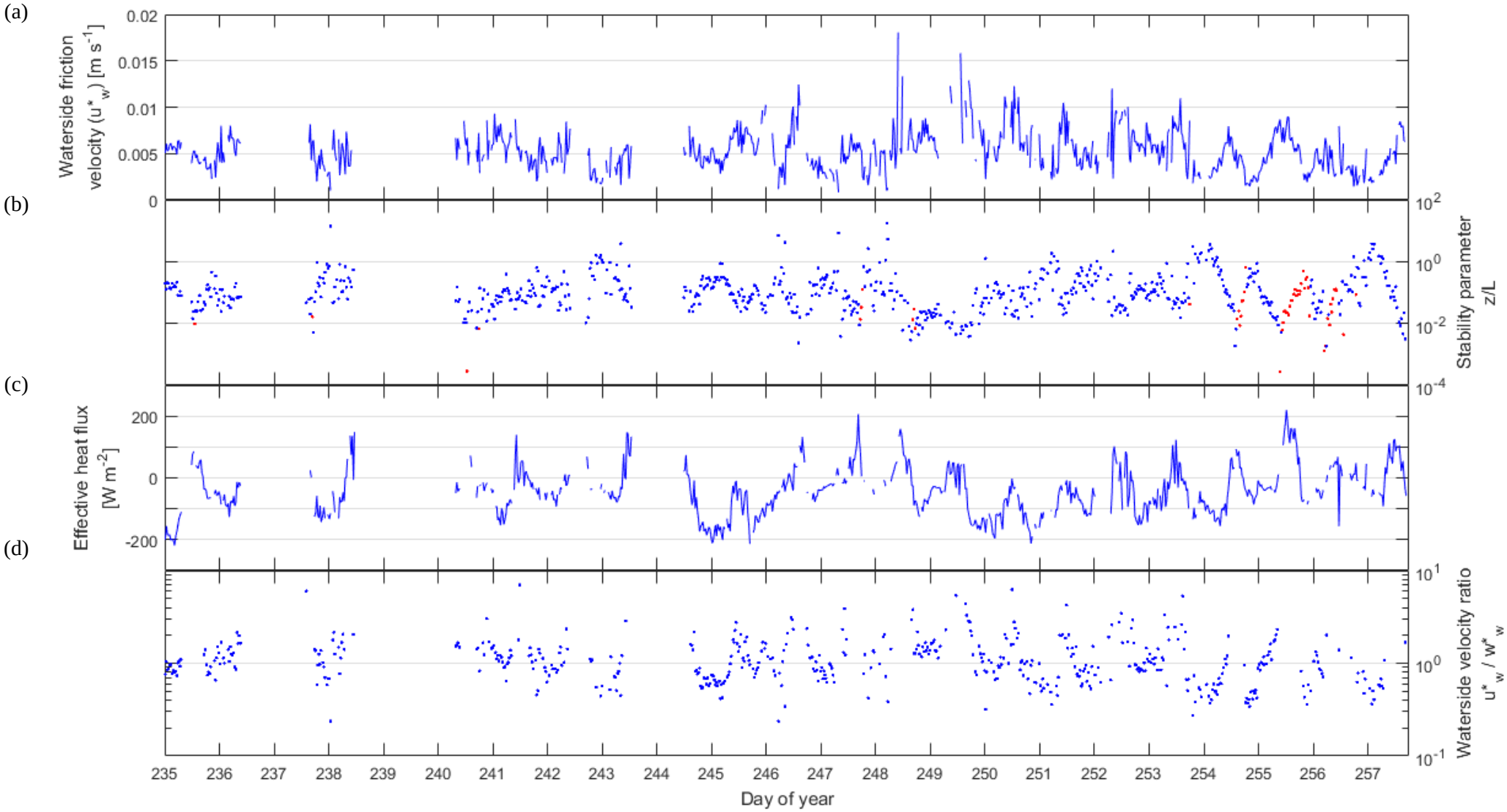

Figure 11. Timeseries of half hour averages of (a) waterside friction velocity (m s^{-1}), (b) atmospheric stability parameter (red for positive values and blue for negative), (c) the ratio of waterside velocity (u^*_w/w^*_w), and (d) effective heat flux (W m^{-2}). The y-axis in (b) and (d) are in logarithm scale. Dateticks represent midnight.

4.2 The conversion to deposition velocity

The O_3 flux measured on the lake platform had mostly negative values (Figure 12a), indicating an overall sink of O_3 from the atmosphere to the lake. The maximum downward flux was 4.2 ppb m s^{-1}. However, it occasionally showed opposite emissions from the lake with a maximum of 1.3 ppb m s^{-1}. The data were more scattered in the first half of the measurement period when the data were omitted for a few individual days due to the spike removal. No observable pattern was found in this dataset. At the same measurement platform, the O_3 concentration was recorded continuously in the entire period (Figure 12b). The local concentration has a clear daily pattern, higher in the daytime and lower in the nighttime. The maximum of 40.9 ppb was detected on day 255 while the lowest of 1.2 ppb was found on day 241. The overall data of O_3 flux and O_3 concentration did not appear to be dependent with each other, as shown in the scatter plot Figure 12d.

By normalizing O_3 flux by O_3 concentration, O_3 deposition velocity was calculated in Figure 12c, the topic parameter in the study. More than 90% of the calculated O_3 deposition velocity fell in the range of 0–5 mm s^{-1}. More scattered and higher velocities were found in the first half of the period, most of which happened in the nighttime. The maximum O_3 deposition velocity of 12.17 mm s^{-1} was found on day 241 due to the incredibly low O_3 concentration. It represented a very high O_3 deposition rate within a single measurement resolution. The calculation resulted in some negative velocities, down to –3.83 mm s^{-1}, meaning an opposite movement of O_3. Despite the irregular weather episodes in the second half of the measurement period (Day 248–249: wind shear domination, day 250–255: air temperature drastic drop and day 254–256: stable atmospheric conditions in the daytime), described in Section 4.1, the deposition process did not vary a lot.

Since O_3 deposition velocity is the quotient of O_3 flux by O_3 concentration, the two variables, O_3 deposition velocity and concentration, were, to some extent, expected to be inversely proportional. Such relationship is clearly observed in Figure 12e when O_3 deposition velocity is in its logarithm form. The graph can be separated by three regions based on the distribution of the values of the solar elevation angle as shown in the color bar. The upper left corner dominated by dark blue represents the lake has a high O_3 deposition velocity but a relatively low concentration in the nighttime. The lower right corner denotes an opposite feature, i.e., high O_3 concentration but low deposition velocity in the daytime (dominated by bright color). The central region is the mixture of the two extremes, where neutral colors are found with moderate deposition velocity and concentration.

(a)

(b)

(c)

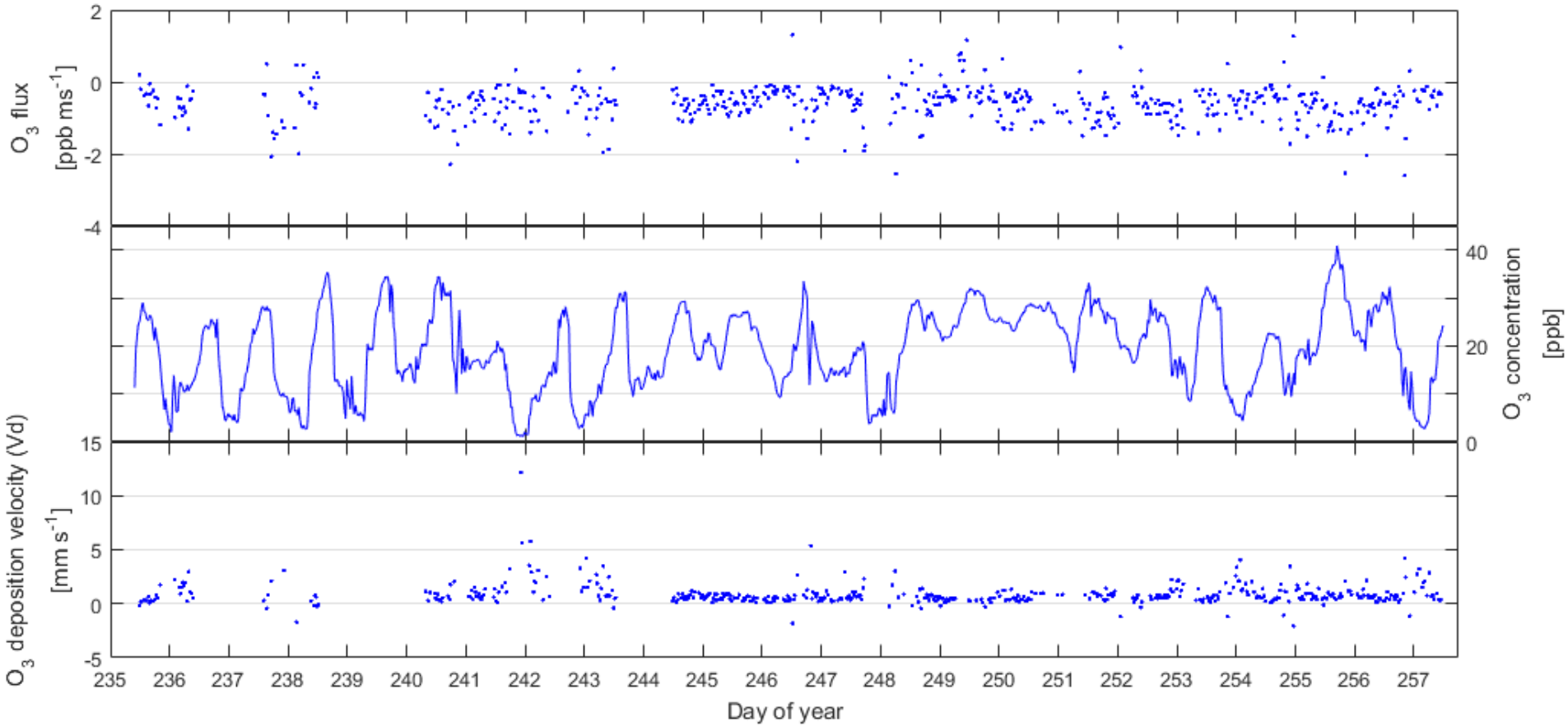

Figure 12. Timeseries of half hour averages of (a) O_3 flux (ppb m s^{-1}), (b) O_3 concentration (ppb), and (c) the calculated O_3 deposition velocity (mm s^{-1}). Dateticks represent midnight.

(d)

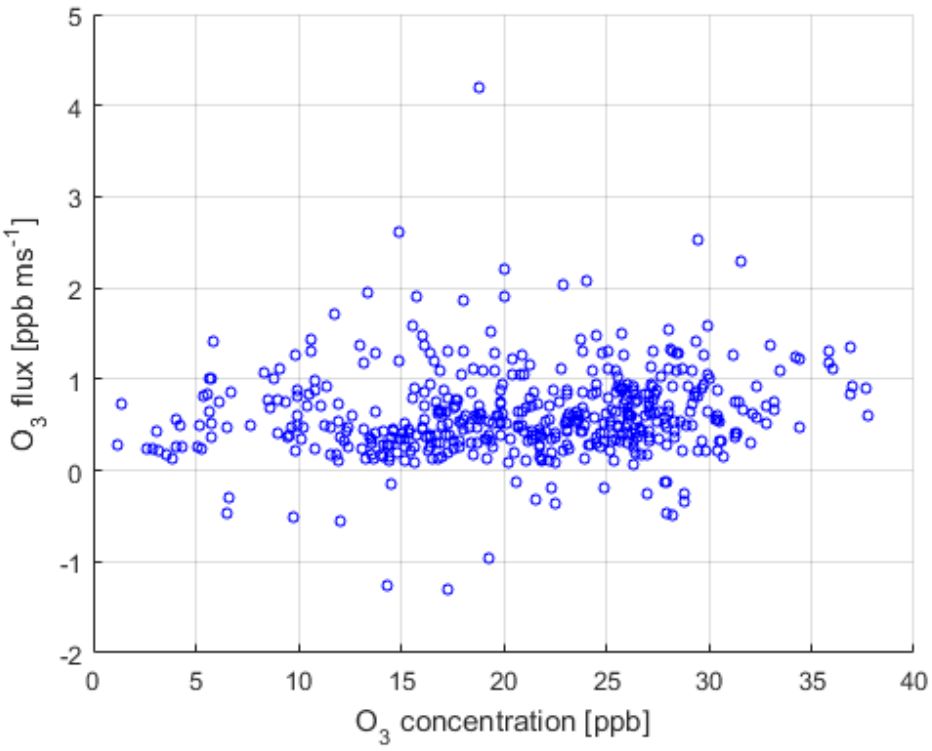

(e)

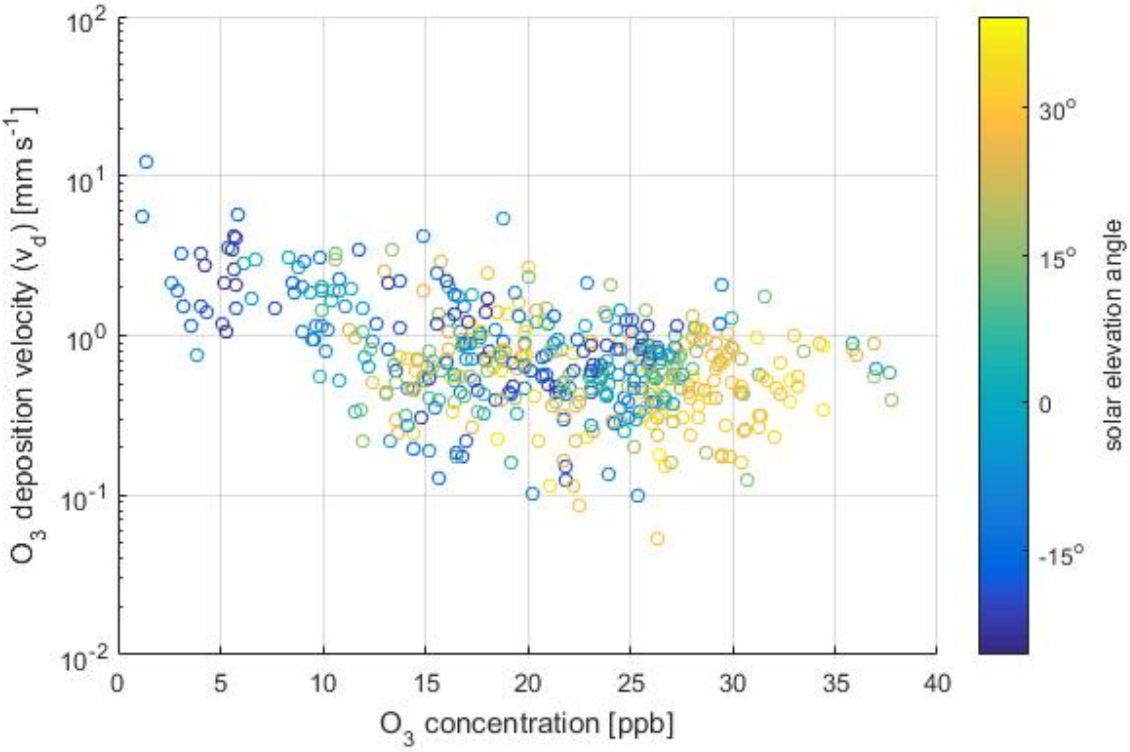

Figure 12. Scatter plots of (d) O_3 flux (ppb m s^{-1}) vs O_3 concentration (ppb), and (e) O_3 velocity deposition (mm s^{-1}) vs O_3 concentration (ppb). The y-axis in (e) is in logarithm scale and its color bar represents solar elevation angle.

4.3 Comparison of forest and lake deposition velocity

From Table 2 and Figure 13, the mean value of deposition velocity was 0.86±0.05 mm s^{-1} for lake measurement, which fell in the expected range, 0.1–1 mm s^{-1}, as summarized by Ganzeveld et al. (2009). The mean averaging O_3 deposition velocity from the SMEAR II station was 4.37±0.08 mm s^{-1}, comparable to the standard value of ~4 mm s^{-1} (Hauglustaine et al., 1994), with a five-fold larger magnitude on average (Figure 13a). The O_3 deposition velocity daily pattern of lake and forest were similar in the entire measurement period, although they have 1000-time difference in roughness length (Seinfeld and Pandis, 2016). Local peaks were found on day 242–243 and 248–249 for tower measurement. Correspondingly, similar peaks were also detected on day 241–243 and 247–248, with a smaller amplitude in the lake measurement, one day slightly ahead of the tower data. The two measurement sites were only few hundred meters away from each other and the lake was surrounded by the forest. Since only the data with wind direction along the lake were considered, the fetch is long enough to ignore the influence by the development of internal boundary layer due to a change in roughness length, on the daily averaged graph. It is reasonable that the two environments experienced almost identical meteorological conditions and that they were interdependent of each other. However, the lagging phenomenon could not be well understood.

The diurnal cycle, on the other hand, shows a different characteristic (Figure 13b). The mean data from the tower had a range from 1.53 mm s^{-1} during the night to 7.70 mm s^{-1} in the daytime. This diurnal cycle is distinct and could be explained by stomatal uptake (Fan et al., 1990; Suni et al., 2003a) and high values in daytime friction velocity (Sun and Massman, 1999; Lamaud et al., 2002). Lake data had a trough of 0.20 mm s^{-1} during the day and a peak at night of 2.28 mm s^{-1} with a greater fluctuation. The higher values in the nighttime might have resulted from the convective mixing of air above a waterbody or the cooling of an uppermost water column, enhancing the stirring of water (Ganzeveld et al., 2009), which will be tested in Section 4.5. Different from daytime velocity, the difference of the two ecosystems in the nighttime is smaller, which can be explained by the condition of no stomatal uptake. However, at 23.30, i.e., one hour after the peak mean value was recorded, a negative mean velocity of –0.02 mm s^{-1} was detected. The standard error of mean values are also bigger in the nighttime than in the daytime. The great variation of ozone deposition to the water surface might be due to the largest uncertainty in measurement among all surface types, addressed by Hardacre et al. (2015).

(a)

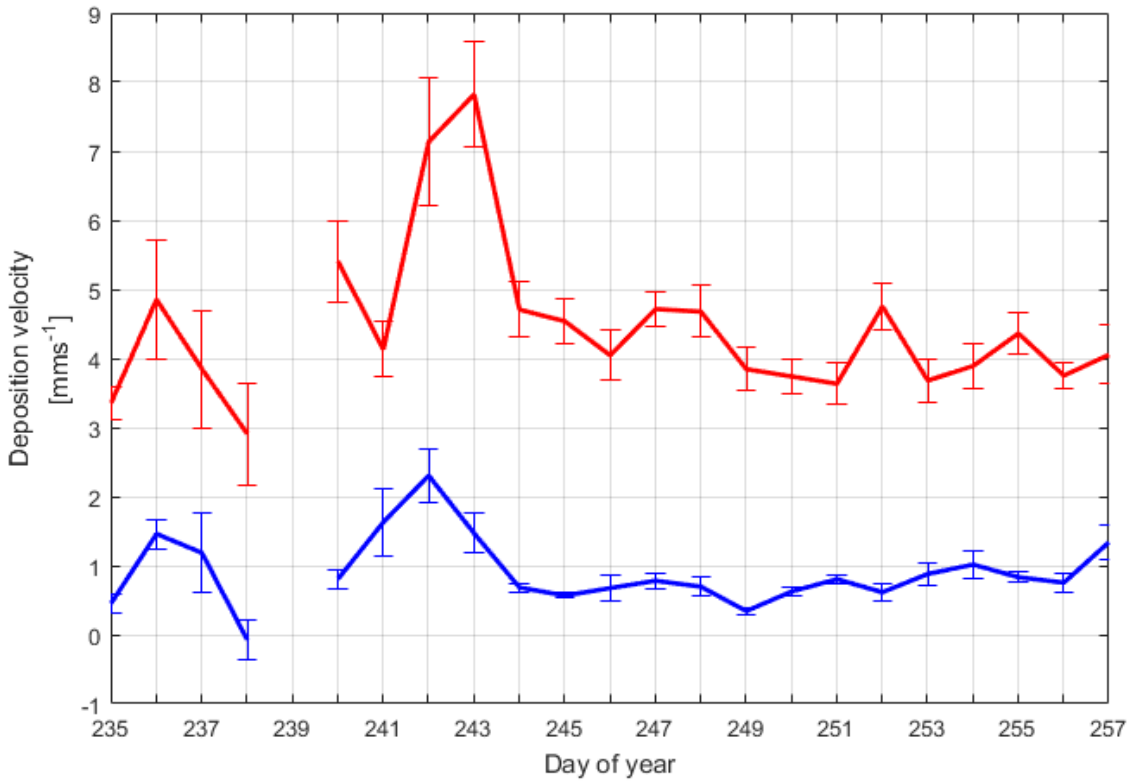

(b)

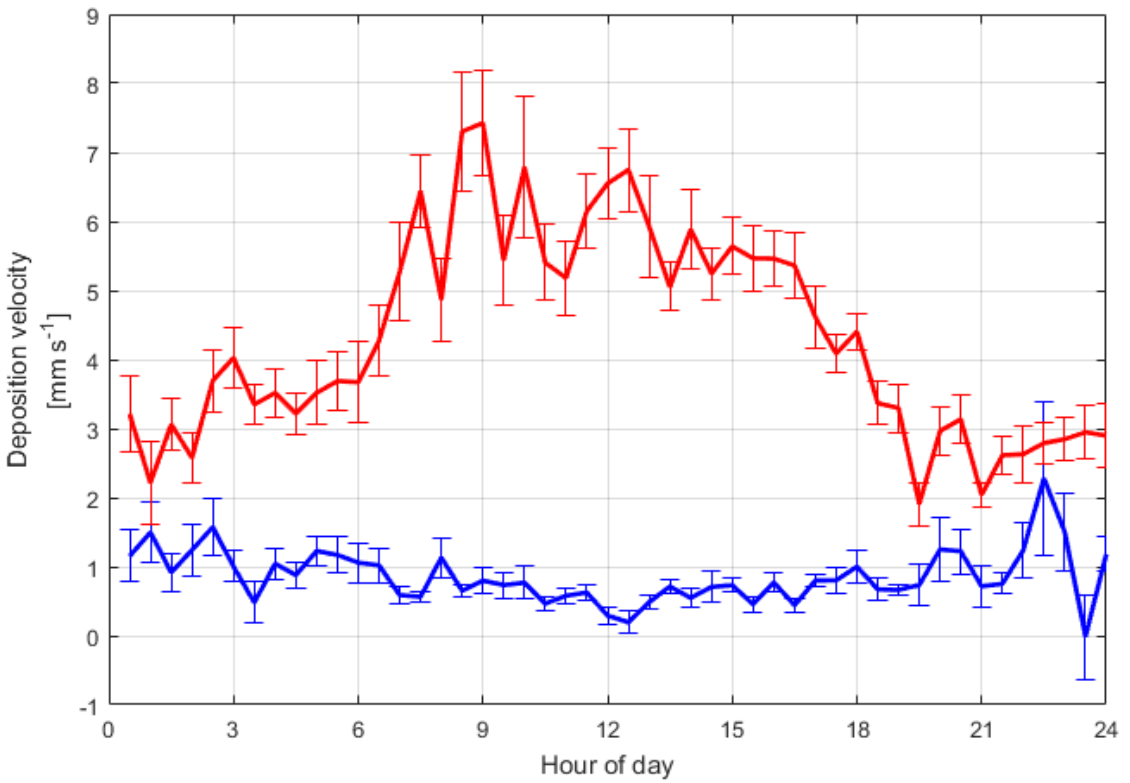

Figure 13. Timeseries of (a) daily mean deposition velocity (mm s^{-1}) and (b) diurnal variation of half-hour mean deposition velocity (mm s^{-1}). Red line represents data from Hyytiälä forest. Blue line shows the measurement from the lake platform. Standard error of mean values are presented as error bars.

Another way to portray the data from the two sites is shown in Figure 13c. The O_3 deposition velocity from the lake platform (in logarithmic form) and forest tower does not show obvious dependency; however, a clear separation by the solar elevation angle is noticeable. A domination of dark blue scatters is found at the upper left corner, which implies the lake has a relatively high O_3 deposition velocity while the nearby forest has a low one during the nighttime. Similar domination of warm color is located at the lower right corner with a wider spread of area. This illustrates an opposite feature from the nighttime. The results from the scatter plot match with the two time-averaged plots above.

(c)

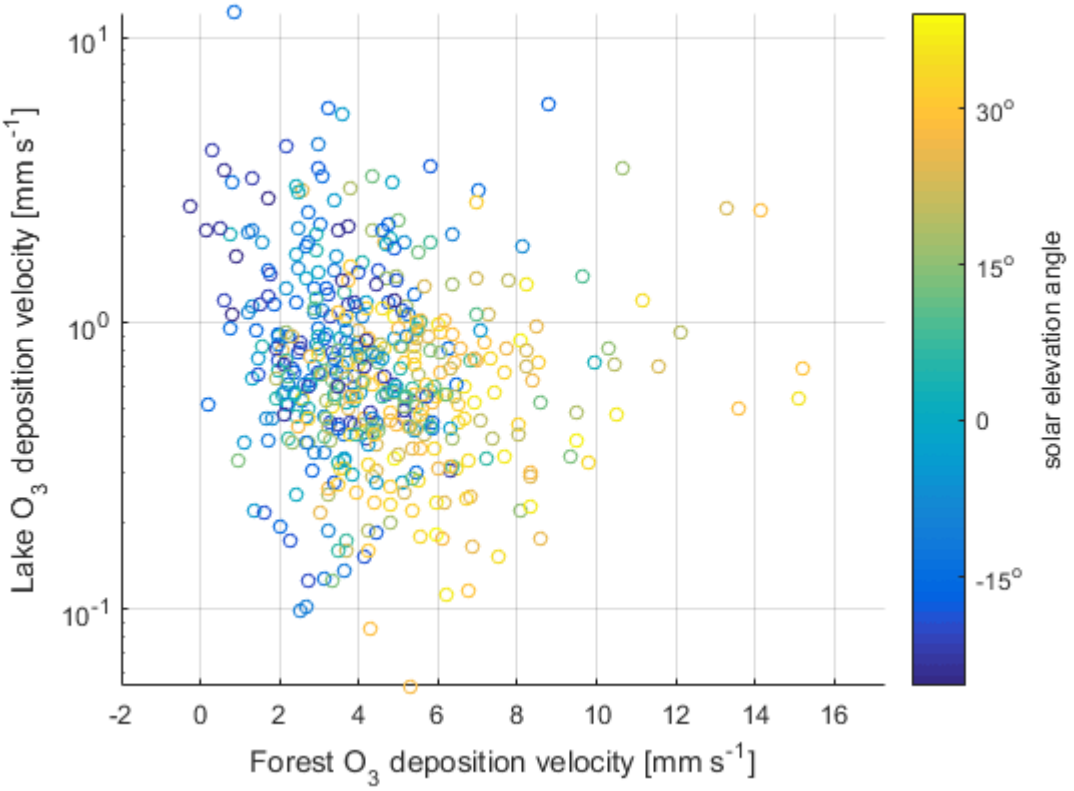

Figure 13c. Scatter plot of lake O_3 velocity deposition (mm s^{-1}) vs forest O_3 velocity deposition (mm s^{-1}). The y-axis is in logarithm scale and its color bar represents Solar elevation angle.

	All			Day			Night			
	Median		Mean	Median		Mean	Median		Mean	U test
v_d [mm s^{-1}]	**0.64**	**+0.39 –0.23**	**0.88±0.05**	**0.57**	**+0.26 –0.18**	**0.70±0.04**	**0.82**	**+0.55 –0.35**	**1.12±0.10**	**h=1, p=2.14 x10^{-6}**
v_d /u*$_w$	**0.12**	**+0.10 –0.05**	**0.20±0.01**	**0.11**	**+0.06 –0.04**	**0.15±0.01**	**0.17**	**+0.19 –0.08**	**0.29±0.03**	**h=1, p=2.41 x10^{-7}**
v_d /U (x10^{-3})	**0.26**	**+0.28 –0.10**	**0.58±0.05**	**0.23**	**+0.17 –0.09**	**0.41±0.04**	**0.35**	**+0.61 –0.15**	**0.87 ±0.12**	**h=1, p=4.64 x10^{-8}**

Table 2. Medians and means of O_3 deposition velocities and the two normalized velocity quantities with all data shown in the second and third column. Daytime and nighttime condition are also included from the fourth to seventh column. Results of Mann-Whitney U test comparing differences between daytime and nighttime velocity quantities are given in U test column. Uncertainties are given as 25th and 75th percentiles for median velocities and as standard errors for the mean quantities.

4.4 Driving force analysis

The deposition velocity under daytime and nighttime condition, as determined by the solar elevation angle (–2°), shows statistically different characteristics. The normalization by the friction velocity (u^*_w) and wind speed (U) were applied to minimize the wind effect on the deposition velocity. All three forms of the deposition velocity (the original and the two normalized velocities) had distinct distributions between day and night, as verified by the Mann–Whitney U tests. Considering all the data, the p-values of three quantities have magnitudes from 10^{-6} to 10^{-8}, which implies they differ from each other statistically at the 95% confidence level (Table 2). Because of this, an analysis for the two conditions separately is required.

In this section, I present boxplots of velocity quantities against the wind speed (U), waterside friction velocity (u^*_w), relative humidity, stability parameter, effective heat flux and waterside velocity scale ratio (u^*_w/w^*_w). Other variables, such as the air temperature, water surface temperature, buoyancy flux, waterside buoyancy velocity and net longwave and shortwave radiation, were once included as part of this analysis, but are not shown here.

Based on Table 2, u^*_w normalized velocity might show a more reasonable diurnal pattern. Therefore, u^*_w normalized velocity was used in the analysis for relative humidity, stability parameter and effective heat flux. The original deposition velocity was plotted against U, u^*_w and waterside scale velocity ratio. Since the dataset in this study is unique and there are only few othersimilar studies on O_3 deposition velocity over freshwater, most comparison were made with CO_2 exchange over freshwater or O_3 over seawater. Hereafter assumptions have to be made such that the physical properties of lake has little/no dependence with the gas species and O_3 performs physically in a similar way in lake as in ocean.

The median values of the deposition velocity were of order of 0.5–0.8 mm s^{-1} and 0.5–1.5 mm s^{-1} at all wind intensity under daytime and nighttime condition respectively (Figure 14). Only under nighttime condition, a weak tendency was found with an increasing wind speed. When the wind speed increased from 0.5 m s^{-1} to 4.5 m s^{-1}, the deposition velocity decreased from 1.4 mm s^{-1} to 0.7 mm s^{-1}. In the daytime, there were no observable trends. This suggests a different view from previous studies of CO_2 exchange over lake or O_3 over seawater (Galbally and Roy, 1980; Kawa and Pearson, 1989; Ganzeveld et al., 2009; Helmig et al., 2012), e.g. that the exchange rate should be higher when

wind speed increases as the constantly moving air can bring away the substance of interest continuously, under both seasonal stratification and overturn condition of water column over lakes (Heiskanen et al., 2014). Other studies (MacIntyre et al., 2001; Podgrajsek et al., 2015) suggested that elevated fluxes were only detected when the wind speed is higher than 5 mm s^{-1}. However, in our study period, the wind speed hardly exceeded 5 m s^{-1} except at occasional data points in daytime condition. No conclusions can be drawn because of this. Boxplots for waterside friction velocity display a similar pattern, which also show disagreement with the abovementioned literature (Figure 15).

What can be clearly seen in Figure 16 is the weak positive tendency of $u*_w$ normalized velocity and relative humidity. The higher the relative humidity, the stronger the deposition velocity. This dependency is more apparent at night. In theory, the role of high water content in the air might be to reduce the surface resistance in the air side, thus obtaining a greater rate of deposition. In addition, the precipitation rate may affect the deposition process for the similar mechanism (Wesely, 1989). During the heavy rain episode on day 246, deposition velocity did not clearly differ from the other dry days (Figure 8f). Therefore, no further analysis of dry and wet conditions was carried out. However, in practice, the elevated relative humidity or precipitation is not supposed to bring any effects on ozone deposition over water surface. Therefore, the reason for the tendency of $u*_w$ normalized velocity and relative humidity remains unknown.

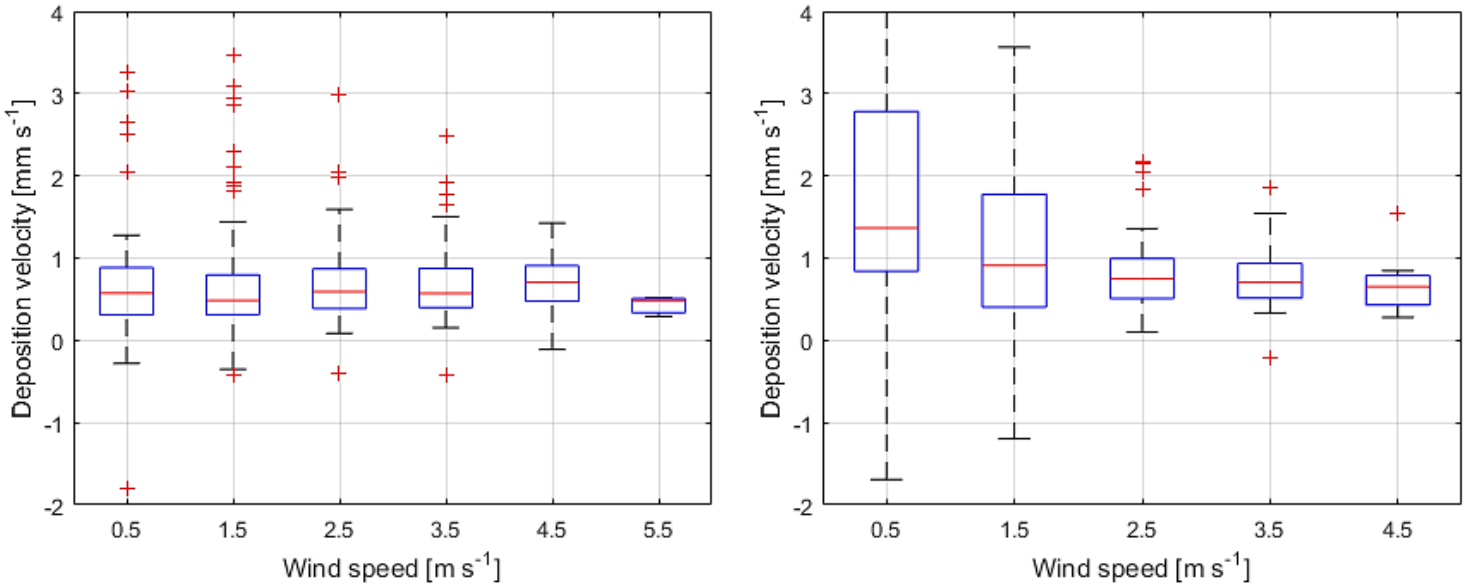

Figure 14. Boxplots of deposition velocity (mm s^{-1}) against binned wind speed (m s^{-1}) in daytime condition (left) and nighttime condition (right) for all data. The data was binned by wind speed, every 1 m s^{-1}, and the bins in the daytime (left) from 0 to 6 m s^{-1} contain about 29, 75, 90, 72, 32 and 3 data points respectively. The bins in the nighttime (right) from 0 to 5 m s^{-1} contain about 24, 85, 48, 19 and 9 data points respectively.

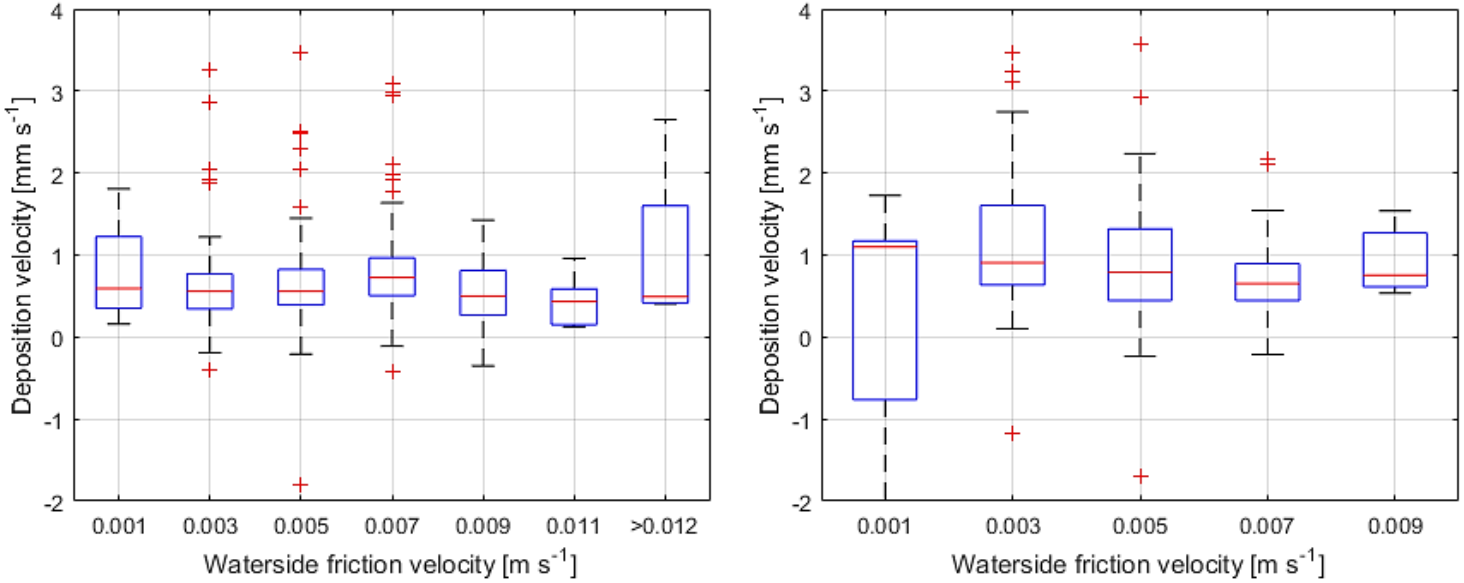

Figure 15. Boxplots of deposition velocity (mm s^{-1}) against binned waterside friction velocity (m s^{-1}) in the daytime (left) and in the nighttime (right) for all data. The data was binned by wind speed, every 0.002 m s^{-1}, except for column >0.012 m s^{-1}. The bins in the daytime (left) from 0 to >0.012 m s^{-1} contain 4, 53, 103, 86, 22, 5 and 4 data points respectively. The bins in the nighttime (right) from 0 to 0.01 m s^{-1} contain 11, 56, 54, 35 and 6 data points respectively.

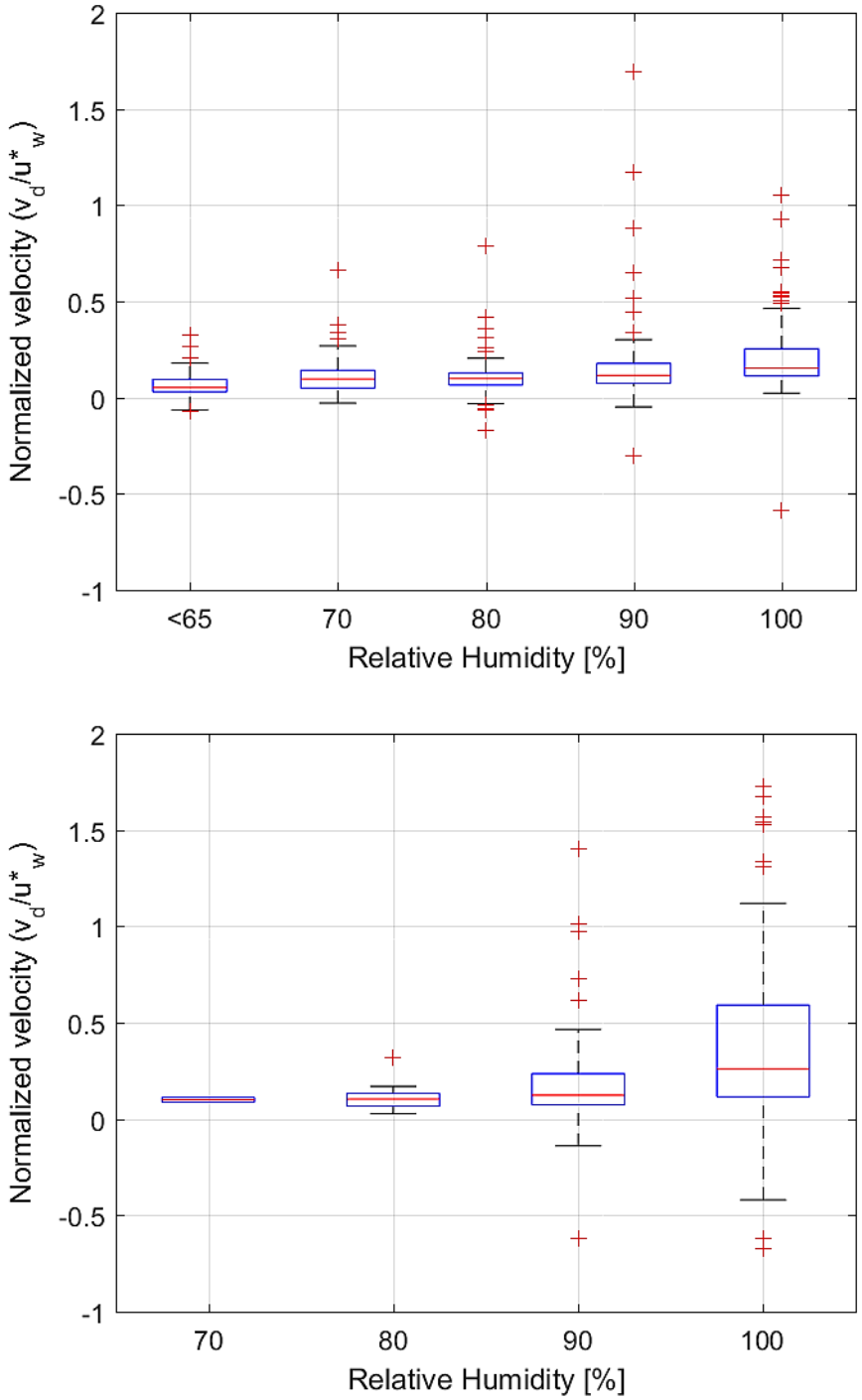

Figure 16. Boxplots of u^*_w normalized velocity against relative humidity (%) in daytime condition (top) and nighttime condition (bottom) for all data. The data was binned by relative humidity, every 10%, except for column <65%. The bins in the daytime (top) from <65% to 105% contain 29, 34, 66, 100 and 72 data points, respectively. The bins in the nighttime (bottom) from 65% to 105% contain 2, 10, 63 and 110 data points, respectively.

Figure 17 reveals that when the atmosphere is classified as unstable during the day, a negative correlation between deposition velocity and atmospheric stability can be found. In the extremely unstable (EU) case (Table 1 on p.19), the average normalized value was as high as 0.6. As it becomes less unstable and even becomes weakly stable, the velocity appears to be rather steady (around 0.1–0.2), except for the case of very stable (VS), which has an unexpectedly high velocity of 1.2. However, this could be explained by the lack of data in this class. During the night, there is a similar pattern on the 'unstable' side as in the daytime, i.e., the velocity drops as it becomes less unstable, but faster (from 1.1 for EU to 0.1 for weakly unstable (WU)). On the 'stable' side, the graph demonstrates a chaotic shape as some studies showed EC flux measurements may experience uncertainties under atmospheric stable conditions (Massman and Lee, 2002; Eugster et al., 2003; Aubinet, 2008) or simply due to insufficient data. The median lines of the normalized ozone deposition velocity generally suggest that unstable conditions in the atmosphere enhance the deposition process as the role of buoyancy outweighs that of shear and triggers vertical motions in the atmosphere. In neutral or stable conditions when the atmosphere tends to be stratified, the deposition process becomes steady. Podgrajsek et al. (2015) even suggested to discard all data obtained under stable conditions. The dependency of atmospheric stability on ozone deposition in unstable conditions might be contributed to flux and concentration footprint. Leclerc and Thurtell (1990) proved that in unstable conditions the peak location and its amplitude tend to be closer to the receptor and larger, respectively. The homogeneous fetch, generally in all wind directions, has to be longer in stable/ neutral conditions than in unstable conditions, in order for a high representativeness (80%) of flux data (Kljun et al., 2002; Mammarella et al., 2015), illustrated by the concept of cumulative footprint function (Gash, 1986; Schuepp et al., 1990).

The effective heat flux, which represents the stability of the uppermost water column, does not show significant dependency of atmospheric stability on ozone deposition (Figure 18). The median lines are almost constant in the daytime graph, ranging from 0.1–0.2, regardless the signs of effective heat flux. The data on effective heat flux at night is mostly negative which does not show any observable tendency either (0.1–0.3). This contradicts the findings by Ganzeveld et al. (2009) who suggested that near-surface mixing causes an increase in the ozone deposition rate. The mixing in the uppermost water column can be escalated by a negative effective heat flux, which indicates a cooling effect on the lake. Yet, from our results, whether the convective mixing due to penetration of solar radiation is boosting or diminishing, it has no visible effect on the deposition process. However, the independence from effective heat flux resembles the results demonstrated in a paper for CO_2 during water column overturn period (Heiskanen et al., 2014). Meanwhile, they demonstrated the correlation with

buoyancy flux in stratified condition. However, this comparison might be not specific enough as our study was in the transition period from stratification to overturn, which would illustrate both characteristics. Another likely explanation is that chemical enhancement on CO_2 and O_3 by effective heat flux might be contrasting as O_3 is less soluble in water and it has much smaller penetration depth, which is on the order of a few μm (Fairall et al., 2007).

Although the effective heat flux does not appear to correlate with O_3 deposition process, the scale of two waterside velocities, u^*_w and w^*_w, displays a stronger correlation with the deposition velocity (Figure 19). From the daytime boxplot, an obvious correlation is not found. However, it appears to have a clear dependency in the nighttime graph when u^*_w becomes the dominant factor in waterside turbulence. After combining all the data regardless of the time of the day, the results show a drop in deposition velocity in two segments when the logarithm of the ratio rises from <–0.4 to –0.15 and from 0.15 to 0.45. The ozone deposition velocity remains at 0.75 mm s^{-1} when the ratio of the two scales is within –0.15 and 0.15 range. The trends at the ratio from <–0.4 to 0.45 show a disagreement with the result by Podgrajsek et al. (2015) who evaluated the dependency with his CO_2 data from a Swedish lake where elevated CO_2 transfer velocities were observed for $u^*_w/w^*_w > 0.75$, i.e., $\log(u^*_w/w^*_w)>-0.15$ and Mammarella et al. (2015) who reported similar results. However, there is an increase in deposition velocity when the ratio goes beyond 0.45 which might be attributed to the insufficient data points. To sum up, the domination of buoyancy-induced turbulence in a mixing process may have no influence/enhancement in deposition. Furthermore, during the night when the mixing was mostly driven by mechanically-induced turbulence, the increase in wind shear would resist the deposition process. Despite the results, convective mixing may still take part in the deposition process in shallow lakes, which profoundly controls the values of w^*_w (Podgrajsek et al., 2015).

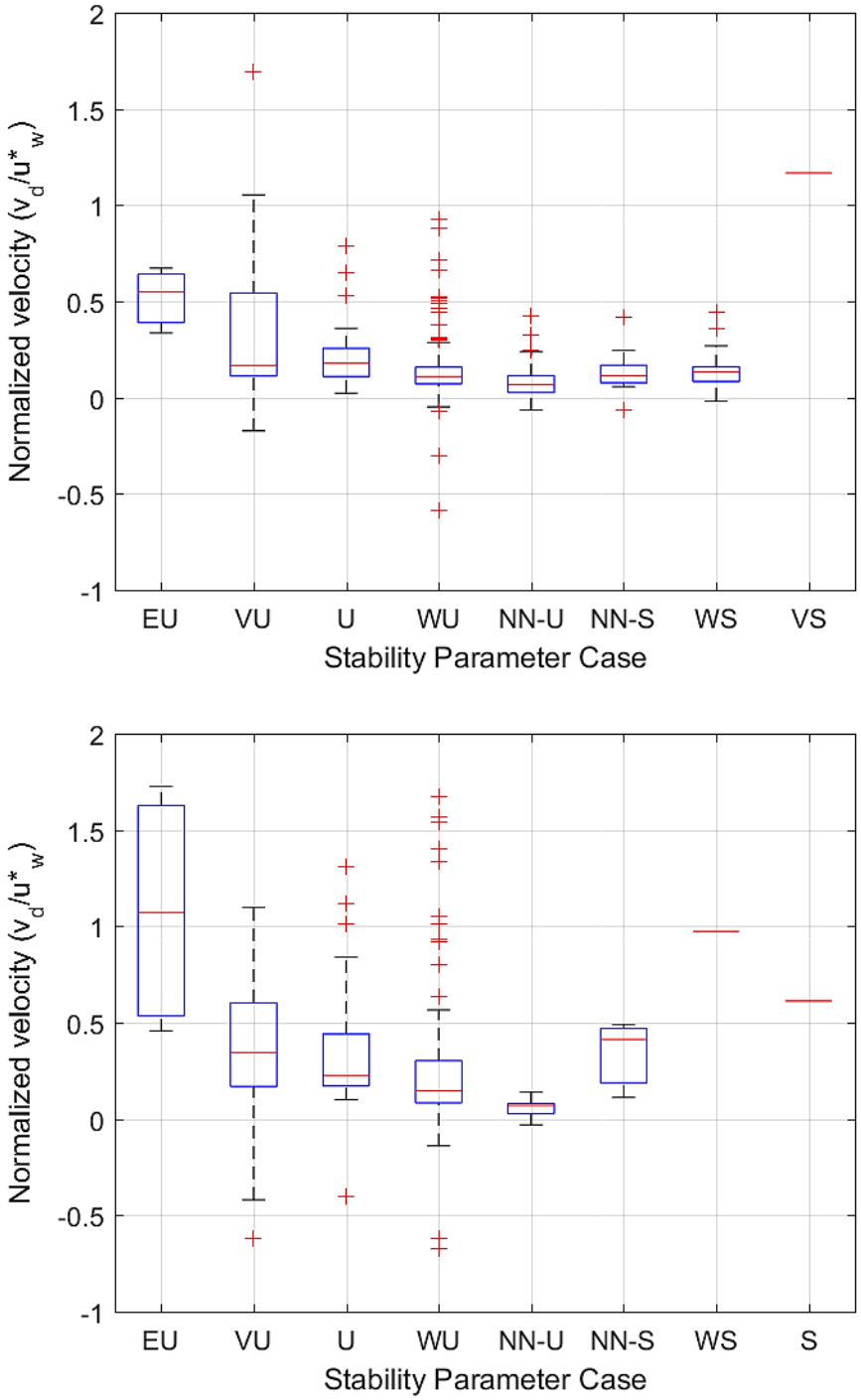

Figure 17. Boxplots of u^*_w normalized velocity against classified stability parameter in daytime condition (top) and nighttime condition (bottom). The stability parameter cases are categorized as in Table 1. The data was binned by each case, and the bins in the daytime (top) from extremely unstable (EU) to very stable (VS) contain 3, 8, 29, 162, 37, 13, 24 and 1 data points, respectively. The bins in the nighttime (bottom) from extremely unstable (EU) to stable (S) contain 4, 21, 25, 99, 8, 3, 1 and 1 data points, respectively.

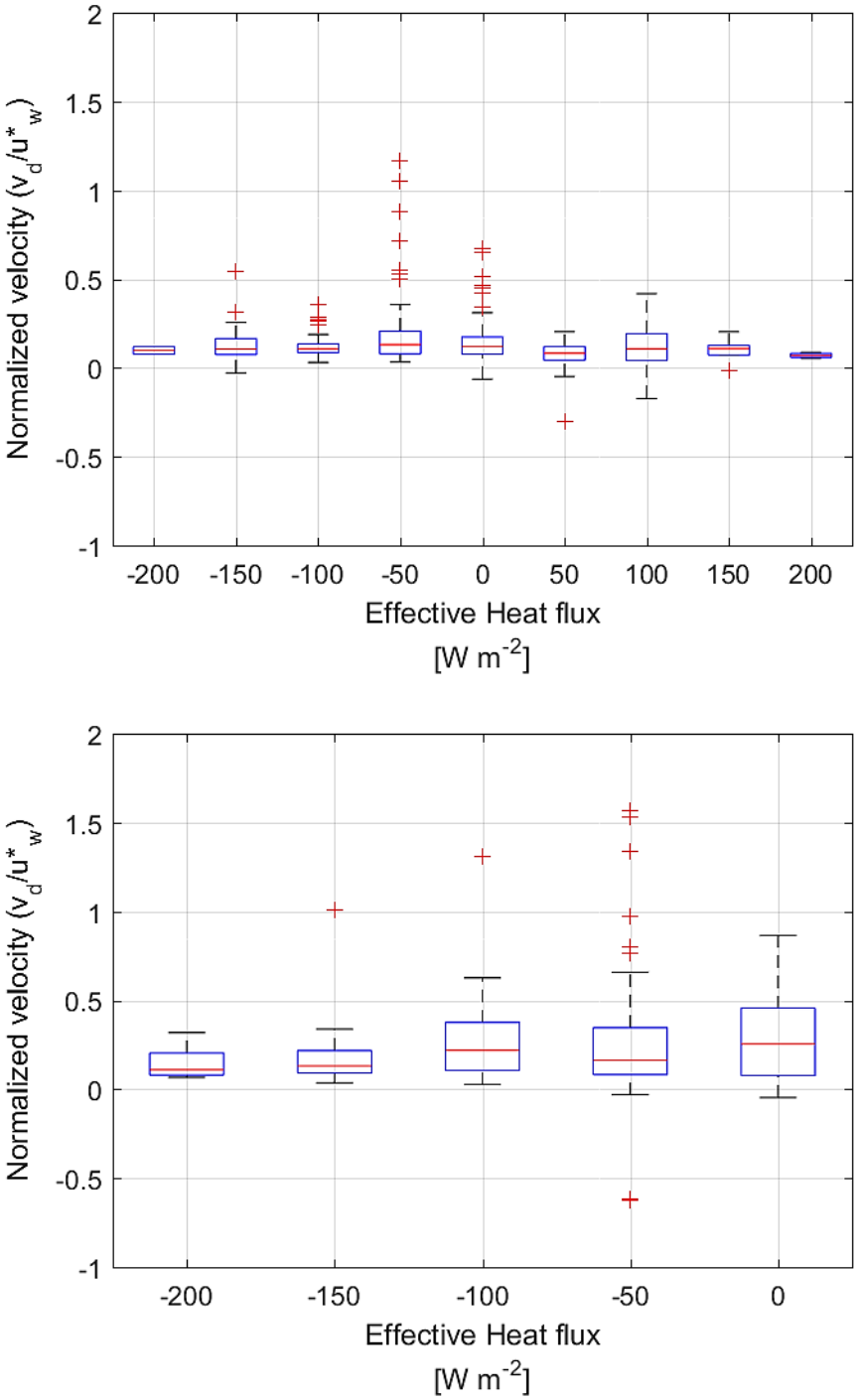

Figure 18. Boxplots of u^*_w normalized velocity against effective heat flux (W m^{-2}) in daytime condition (top) and nighttime condition (bottom). The data was binned by effective heat flux, every 50 W m^{-2}, and the bins in the daytime (top) from –225 to 225 W m^{-2} contain 2, 21, 39, 65, 66, 52, 16, 12 and 4 data points respectively. The bins in the nighttime (bottom) from –225 to 25 W m^{-2} contain 10, 32, 46, 70 and 8 data points respectively.

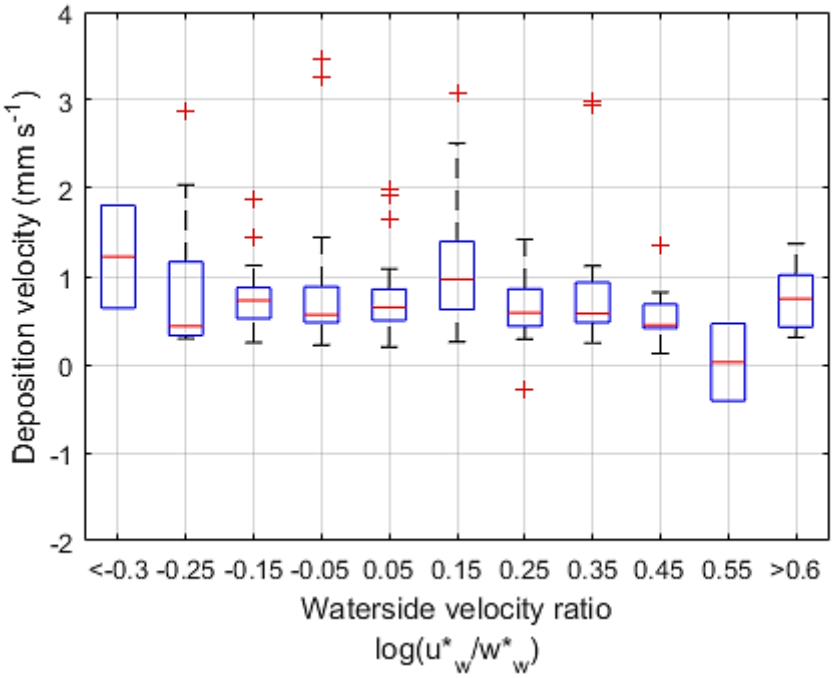

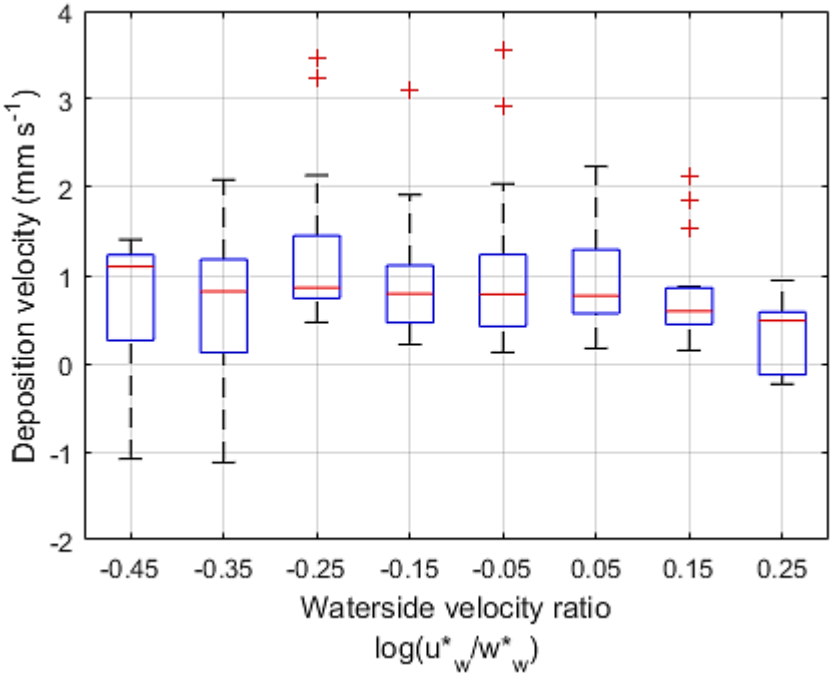

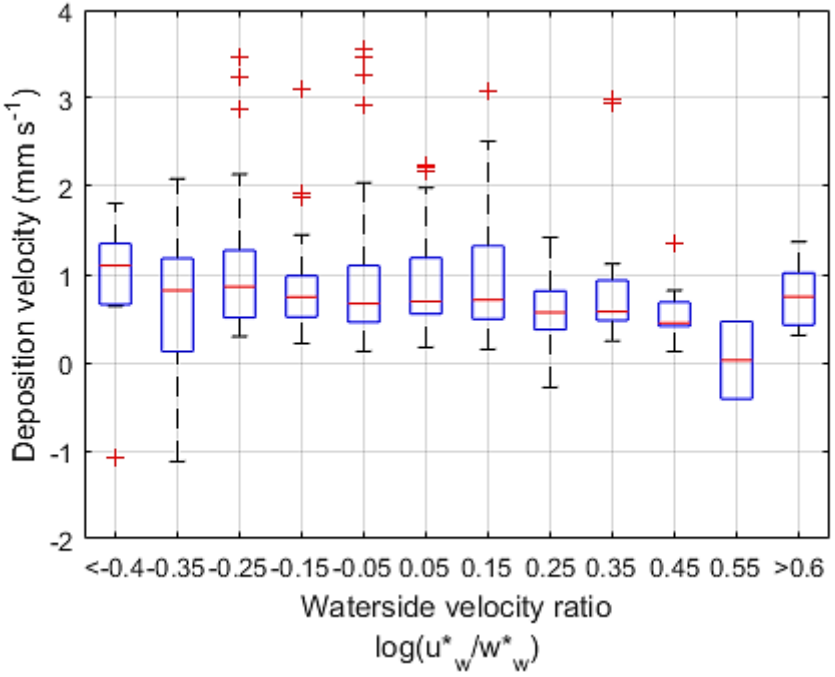

Figure 19. Boxplots of deposition velocity (mm s^{-1}) against the logarithm of waterside velocity scale ratio in daytime condition (top left), nighttime condition (top right) and all data (bottom). Positive values represent mechanically-induced turbulence dominates the convection process in water column and negative values show buoyancy domination. The data was binned by the logarithm of waterside velocity scale ratio. The bins in daytime data (top left) from <–0.3 to >0.6 contain 2, 10, 19, 27, 21, 20, 22, 17, 11, 2 and 5 data points respectively. The bins in nighttime data (top right) from –0.45 to 0.35 contain 5, 11, 19, 17, 41, 29, 16 and 7 data points respectively. The bins in all data (bottom) from <–0.4 to >0.6 contain 7, 11, 29, 36, 68, 50, 36, 29, 17, 11, 2 and 5 data points respectively.

5. Conclusions

Meteorological and flux data were recorded at Lake Kuivajärvi, Finland in the measurement campaign which lasted for 43 days in August and September in 2012. Data from the surrounding tower at Hyytiälä forest were also acquired for comparison. The data were processed and only the data with winds blowing along the lake were retained for a further analysis. The flux data were normalized by O_3 concentration for the calculation of O_3 deposition velocity. The data were then separated into daytime and nighttime based on the solar elevation angle (–2°) for driving force analysis. Both the average O_3 deposition velocity over lake and over forest showed diurnal cycles. The daytime and nighttime data differed from each other statistically. Elevated deposition velocities in nocturnal unstable conditions were found as the highlight of the study.

Environmental conditions of the lake were typical for the transition from summer to autumn. The surface water was generally warmer than the air, leading to an overall positive sensible heat flux and negative net longwave radiation. The wind speed, wind direction and friction velocity did not change much during the whole period. The atmosphere was mostly unstable, whereas the uppermost water column tended to have convective mixing due to cooling, proven by the progressively deepening actively mixing layer. However, the turbulence for water mixing was generally dominated by the wind shear. The wind speed, friction velocity and the stability of both atmosphere and uppermost water showed a diurnal cycle. The daytime period tended to have stronger winds, but less unstable conditions in both atmosphere and water column. The mixing in water tended to be more dominated by waterside friction velocity in the daytime.

The O_3 deposition velocity over lake had an average value of 0.88±0.05 mm s^{-1}, comparable to 0.1 to 1 mm s^{-1} reported by Wesely et al. (1981) and Ganzeveld et al. (2009), while that over the nearby forest was 5-time larger (4.37 mm s^{-1}). The daily averaged timeseries in both lake and forest followed the same pattern, with the former apparently one day ahead of the latter. Both showed diurnal cycle but in an opposite manner. The deposition process over the lake took place more vigorously at night (1.12±0.10 mm s^{-1}) than that in the daytime (0.70±0.04 mm s^{-1}), with a difference of 0.42 mm s^{-1}. During the night, the difference of the averaged deposition velocity between lake and forest was smaller. By using Mann-Whitney U test, O_3 deposition velocity in the daytime and nighttime differed statistically.

The O_3 deposition velocity showed a negative tendency with increasing nighttime wind and no correlation with the daytime wind speed, which is inconsistent with most literature on O_3 deposition or CO_2 gaseous exchange process (Galbally and Roy, 1980; Kawa and Pearson, 1989; MacIntyre et al., 2001; Ganzeveld et al., 2009; Helmig et al., 2012; Heiskanen et al., 2014; Podgrajsek et al., 2015). The deposition velocity overall decreased when the dominance of turbulence by waterside friction velocity became stronger, which disagreed with Podgrajsek et al. (2015).

The O_3 deposition velocity was further normalized by the waterside friction velocity to eliminate the other wind effects. It showed a weak positive correlation with relative humidity; however, the reason remains unknown as water content in the atmosphere does not alter the properties of the lake water, the depositing surface. Under atmospheric unstable conditions, both in the daytime and nighttime, lakes had a greater normalized deposition velocity as the role of buoyancy outweighs that of shear and triggers vertical motions in the atmosphere, which intensifies the deposition process. Although only data along the lake was retained for the analysis, footprint in unstable conditions tends to have a closer peak location and higher peak values (Leclerc and Thurtell, 1990; Kljun et al., 2002; Mammarella et al., 2015), which creates a higher representativeness for lake surface. The extent of convective mixing due to cooling, demonstrated by effective heat flux, did not show any visible correlation with normalized deposition velocity, which contradicted Ganzeveld et al. (2009) and Heiskanen et al. (2014).

Nevertheless, due to the uniqueness of the dataset and the inadequate amount of previous relevant studies, no direct comparisons can be made. Some were done with paper on CO_2 exchange over lake or O_3 deposition over ocean. The physical properties of lake was assumed to have little/ no dependence with the gas species. O_3 was also assumed to perform physically in a similar way in lake as in ocean. Morevoer, lakes with different characteristics may respond differently to various physical forcing (Podgrajsek et al., 2015). Despite all these issue, this thesis on the topic of 'ozone deposition process over boreal lake using EC techniques' could serve as a continual work of Wesely (1981) and a reference for researchers who explore O_3 deposition process over freshwater in the future.

6. Reference

Atkinson, R., & Aschmann, S. M. (1993). Hydroxyl radical production from the gas-phase reactions of ozone with a series of alkenes under atmospheric conditions. *Environmental science & technology*, 27(7), 1357-1363.

Antonia, R. A., & Luxton, R. E. (1972). The response of a turbulent boundary layer to a step change in surface roughness. Part 2. Rough-to-smooth. *Journal of Fluid Mechanics*, *53*(4), 737-757.

Aubinet, M. (2008). Eddy covariance CO2 flux measurements in nocturnal conditions: an analysis of the problem. *Ecological Applications*, *18*(6), 1368-1378.

Aubinet, M., Vesala, T., & Papale, D. (Eds.). (2012). *Eddy covariance: a practical guide to measurement and data analysis*. Springer Science & Business Media.

Boegman, L., Ivey, G. N., & Imberger, J. (2005). The degeneration of internal waves in lakes with sloping topography. *Limnology and oceanography*, *50*(5), 1620-1637.

Bäck, J., Aalto, J., Henriksson, M., Hakola, H., He, Q., & Boy, M. (2012). Chemodiversity of a Scots pine stand and implications for terpene air concentrations. *Biogeosciences*, *9*(2), 689-702.

Brutsaert, W. (1982). Energy Budget and Related Methods. In *Evaporation into the Atmosphere* (pp. 209-230). Springer, Dordrecht.

Burba, G., & Anderson, D. (2007). Introduction to the eddy covariance method: General guidelines and conventional workflow. *Li-Cor Biosciences*, *141*.

Caraco, N.F., Melack, J.M., & Middelburg, J. J. (2006). The global abundance and size distribution of lakes, ponds, and impoundments. *Limnology and Oceanography*, *51*(5), 2388-2397.

Chang, W., Heikes, B. G., & Lee, M. (2004). Ozone deposition to the sea surface: chemical enhancement and wind speed dependence. *Atmospheric Environment*, *38*(7), 1053-1059.

Claussen, M. (1991). Estimation of areally-averaged surface fluxes. *Boundary-Layer Meteorology*, *54*(4), 387-410.

Clifford, D., Donaldson, D. J., Brigante, M., D'Anna, B., & George, C. (2008). Reactive uptake of ozone by chlorophyll at aqueous surfaces. *Environmental science & technology*, *42*(4), 1138-1143.

Contreras Iglesias, S. (2003). *Degradation and biodegradability enhancement of nitrobenzene and 2, 4-dichlorophenol by means of Advanced Oxidation Processes based on ozone*. Universitat de Barcelona.

Crill, P. M., Bartlett, K. B., Harriss, R. C., Gorham, E., Verry, E. S., Sebacher, D. I., Madzar, L., & Sanner, W. (1988). Methane flux from Minnesota peatlands. *Global Biogeochemical Cycles*, *2*(4), 371-384.

Downing, J. A., Prairie, Y. T., Cole, J. J., Duarte, C. M., Tranvik, L. J., Striegl, R. G., McDowell, W.H., Kortelainen, P.,

Deacon, E. L. (1977). Gas transfer to and across an air-water interface. *Tellus*, *29*(4), 363-374.

Erkkilä, K. M., Ojala, A., Bastviken, D., Biermann, T., Heiskanen, J. J., Lindroth, A., Peltola, O., Rantakari, M., Vesala, T., & Mammarella, I. (2018). Methane and carbon dioxide fluxes over a lake: comparison between eddy covariance, floating chambers and boundary layer method. *Biogeosciences*, *15*(2), 429-445.

Eugster, W., Kling, G., Jonas, T., McFadden, J. P., Wüest, A., MacIntyre, S., & Chapin, F. S. (2003). CO2 exchange between air and water in an Arctic Alaskan and midlatitude Swiss lake: Importance of convective mixing. *Journal of Geophysical Research: Atmospheres*, *108*(D12).

Eugster, W., DelSontro, T., & Sobek, S. (2011). Eddy covariance flux measurements confirm extreme CH (4) emissions from a Swiss hydropower reservoir and resolve their short-term variability. *Biogeosciences*, *8*(9), 2815-2831.

Fairall, C. W., Helmig, D., Ganzeveld, L., & Hare, J. (2007). Water-side turbulence enhancement of ozone deposition to the ocean. *Atmospheric Chemistry and Physics*, *7*(2), 443-451.

Fan, S. M., Wofsy, S. C., Bakwin, P. S., Jacob, D. J., & Fitzjarrald, D. R. (1990). Atmosphere-biosphere exchange of CO_2 and O_3 in the central Amazon forest. *Journal of Geophysical Research: Atmospheres*, *95*(D10), 16851-16864.

Foken, T. (2008). The energy balance closure problem: an overview. *Ecological Applications*, *18*(6), 1351-1367.

Galbally, I. E., & Roy, C. R. (1980). Destruction of ozone at the earth's surface. *Quarterly Journal of the Royal Meteorological Society*, *106*(449), 599-620.

Ganzeveld, L., Helmig, D., Fairall, C. W., Hare, J., & Pozzer, A. (2009). Atmosphere-ocean ozone exchange: A global modeling study of biogeochemical, atmospheric, and waterside turbulence dependencies. *Global Biogeochemical Cycles*, *23*(4).

Garland, J. A., Elzerman, A. W., & Penkett, S. A. (1980). The mechanism for dry deposition of ozone to seawater surfaces. *Journal of Geophysical Research: Oceans*, *85*(C12), 7488-7492.

Gash, J. H. C. (1986). A note on estimating the effect of a limited fetch on micrometeorological evaporation measurements. *Boundary-Layer Meteorology*, *35*(4), 409-413.

Hardacre, C., Wild, O., & Emberson, L. (2015). An evaluation of ozone dry deposition in global scale chemistry climate models. *Atmospheric Chemistry and Physics*, *15*(11), 6419-6436.

Hari, P., Nikinmaa, E., Pohja, T., Siivola, E., Bäck, J., Vesala, T., & Kulmala, M. (2013). Station for measuring ecosystem-atmosphere relations: SMEAR. In *Physical and Physiological Forest Ecology* (pp. 471-487). Springer, Dordrecht.

Hauglustaine, D. A., Granier, C., Brasseur, G. P., & Megie, G. (1994). The importance of atmospheric chemistry in the calculation of radiative forcing on the climate system. *Journal of Geophysical Research: Atmospheres*, *99*(D1), 1173-1186.

Heiskanen, J. J., Mammarella, I., Haapanala, S., Pumpanen, J., Vesala, T., MacIntyre, S., & Ojala, A. (2014). Effects of cooling and internal wave motions on gas transfer coefficients in a boreal lake. *Tellus B: Chemical and Physical Meteorology*, *66*(1), 22827.

Heiskanen, J. J., Mammarella, I., Ojala, A., Stepanenko, V., Erkkilä, K. M., Miettinen, H., ... & Vesala, T. (2015). Effects of water clarity on lake stratification and lake-atmosphere heat exchange. *Journal of Geophysical Research: Atmospheres*, *120*(15), 7412-7428.

Helmig, D., Oltmans, S. J., Carlson, D., Lamarque, J. F., Jones, A., Labuschagne, C., Anlauf, K., & Hayden, K. (2007). A review of surface ozone in the polar regions. *Atmospheric Environment*, *41*(24), 5138-5161.

Helmig, D., Boylan, P., Johnson, B., Oltmans, S., Fairall, C., Staebler, R., Weinheimer, A., Orlando, J., Knapp, D.J., Montzka, D.D., & Flocke, F. (2012). Ozone dynamics and snow-atmosphere exchanges during ozone depletion events at Barrow, Alaska. *Journal of Geophysical Research: Atmospheres*, *117*(D20).

Huotari, J., Ojala, A., Peltomaa, E., Nordbo, A., Launiainen, S., Pumpanen, J., Rasilo, T., Hari, P., & Vesala, T. (2011). Long-term direct CO2 flux measurements over a boreal lake: Five years of eddy covariance data. *Geophysical Research Letters*, *38*(18).

Imberger, J. (1985). The diurnal mixed layer. *Limnology and oceanography*, *30*(4), 737-770.

Jacob, D. (1999). *Introduction to atmospheric chemistry*. Princeton University Press.

Jensen, N. O. (1978). Change of surface roughness and the planetary boundary layer. *Quarterly Journal of the Royal Meteorological Society*, *104*(440), 351-356.

Junninen, H., Lauri, A., Keronen, P., AaIto, P., HiItunen, V., Hari, P., & KuImaIa, M. (2009). Smart-SMEAR: on-line data exploration and visualization tool tor SMEAR stations. *Boreal Environment Research*, *14*(4).

Kaimal, J. C., & Finnigan, J. J. (1994). *Atmospheric boundary layer flows: their structure and measurement*. Oxford university press.

Kawa, S. R., & Pearson, R. (1989). Ozone budgets from the dynamics and chemistry of marine stratocumulus experiment. *Journal of Geophysical Research: Atmospheres*, *94*(D7), 9809-9817.

Kljun, N., Rotach, M. W., & Schmid, H. P. (2002). A three-dimensional backward Lagrangian footprint model for a wide range of boundary-layer stratifications. *Boundary-Layer Meteorology*, *103*(2), 205-226.

Kolari, P., Pumpanen, J., Kulmala, L., Ilvesniemi, H., Nikinmaa, E., Grönholm, T., & Hari, P. (2006). Forest floor vegetation plays an important role in photosynthetic production of boreal forests. *Forest Ecology and Management*, *221*(1-3), 241-248.

Krinner, G. (2003). Impact of lakes and wetlands on boreal climate. *Journal of Geophysical Research: Atmospheres*, *108*(D16).

Kulmala, L., Launiainen, S., Pumpanen, J., Lankreijer, H., Lindroth, A., Hari, P., & Vesala, T. (2008). H2O and CO2 fluxes at the floor of a boreal pine forest. *Tellus B*, *60*(2), 167-178.

Lamarque, J. F., Hess, P., Emmons, L., Buja, L., Washington, W., & Granier, C. (2005). Tropospheric ozone evolution between 1890 and 1990. *Journal of Geophysical Research: Atmospheres*, *110*(D8).

Lamaud, E., Carrara, A., Brunet, Y., Lopez, A., & Druilhet, A. (2002). Ozone fluxes above and within a pine forest canopy in dry and wet conditions. *Atmospheric Environment*, *36*(1), 77-88.

Leclerc, M. Y., & Thurtell, G. W. (1990). Footprint prediction of scalar fluxes using a Markovian analysis. *Boundary-Layer Meteorology*, *52*(3), 247-258.

Lee, X., Massman, W., & Law, B. (Eds.). (2006). *Handbook of micrometeorology: a guide for surface flux measurement and analysis* (Vol. 29). Springer Science & Business Media.

Liss, P. S. (1974). Flux of gases across the air-sea interface. *Nature*, *247*, 181-184.

Lowry, R. (2014). Concepts and applications of inferential statistics.

Luhar, A. K., Galbally, I. E., Woodhouse, M. T., & Thatcher, M. (2017). An improved parameterisation of ozone dry deposition to the ocean and its impact in a global climate-chemistry model. *Atmospheric Chemistry and Physics*, *17*(5), 3749.

MacIntyre, S., Eugster, W., & Kling, G. W. (2001). The critical importance of buoyancy flux for gas flux across the air-water interface. *Gas transfer at water surfaces*, 135-139.

Mammarella, I., Nordbo, A., Rannik, Ü., Haapanala, S., Levula, J., Laakso, H., Ojala, A., Peltola, O., Heiskanen, J., Pumpanen, J., & Vesala, T. (2015). Carbon dioxide and energy fluxes over a small boreal lake in Southern Finland. *Journal of Geophysical Research: Biogeosciences*, *120*(7), 1296-1314.

Mammarella, I., Peltola, O., Nordbo, A., Järvi, L., & Rannik, Ü. (2016). Quantifying the uncertainty of eddy covariance fluxes due to the use of different software packages and combinations of processing steps in two contrasting ecosystems. *Atmospheric Measurement Techniques*, *9*(10), 4915.

Massman, W. J., & Lee, X. (2002). Eddy covariance flux corrections and uncertainties in long-term studies of carbon and energy exchanges. *Agricultural and Forest Meteorology*, *113*(1), 121-144.

McRae, G. J., Goodin, W. R., & Seinfeld, J. H. (1982). Development of a second-generation mathematical model for urban air pollution—I. Model formulation. *Atmospheric Environment (1967)*, *16*(4), 679-696.

Monin, A. S., & Obukhov, A. M. F. (1954). Basic laws of turbulent mixing in the surface layer of the atmosphere. *Contrib. Geophys. Inst. Acad. Sci. USSR*, *151*(163), e187.

Monismith, S. G. (1985). Wind-forced motions in stratified lakes and their effect on mixed-layer shear. *Limnology and oceanography*, *30*(4), 771-783.

Mulhearn, P. J., & Finnigan, J. J. (1978). Turbulent flow over a very rough, random surface. *Boundary-Layer Meteorology*, *15*(1), 109-132.

Nordbo, A., Launiainen, S., Mammarella, I., Leppäranta, M., Huotari, J., Ojala, A., & Vesala, T. (2011). Long-term energy flux measurements and energy balance over a small boreal lake using eddy covariance technique. *Journal of Geophysical Research: Atmospheres*, *116*(D2).

Oltmans, S. J., Lefohn, A. S., Scheel, H. E., Harris, J. M., Levy, H., Galbally, I. E., Brunke, E.G., Meyer, C.P., Lathrop, J.A.,

Johnson, B.J., & Shadwick, D. S. (1998). Trends of ozone in the troposphere. *Geophysical Research Letters*, *25*(2), 139-142.

Podgrajsek, E., Sahlée, E., & Rutgersson, A. (2014). Diurnal cycle of lake methane flux. *Journal of Geophysical Research: Biogeosciences*, *119*(3), 236-248.

Podgrajsek, E., Sahlée, E., & Rutgersson, A. (2015). Diel cycle of lake-air CO2 flux from a shallow lake and the impact of waterside convection on the transfer velocity. *Journal of Geophysical Research: Biogeosciences*, *120*(1), 29-38.

Raatikainen, M., & Kuusisto, E. (1990). The number and surface area of the lakes in Finland. *Terra*, *102*(2), 97-110.

Rannik, Ü., Mammarella, I., Keronen, P., & Vesala, T. (2009). Vertical advection and nocturnal deposition of ozone over a boreal pine forest. Atmospheric Chemistry and Physics, 9(6), 2089-2095.

Rannik, Ü., Altimir, N., Mammarella, I., Bäck, J., Rinne, J., Ruuskanen, T. M., Hari, P., Vesala, T., & Kulmala, M. (2012). Ozone deposition into a boreal forest over a decade of observations: evaluating deposition partitioning and driving variables. *Atmospheric Chemistry and Physics*, *12*(24), 12165-12182.

Read, J. S., Hamilton, D. P., Desai, A. R., Rose, K. C., MacIntyre, S., Lenters, J. D., Smyth, R.L., Hanson, P.C., Cole, J.J., Staehr, P.A., & Rusak, J. A. (2012). Lake-size dependency of wind shear and convection as controls on gas exchange. *Geophysical Research Letters*, *39*(9).

Samuelsson, P., Kourzeneva, E., & Mironov, D. (2010). The impact of lakes on the European climate as stimulated by a regional climate madel. *Boreal environment research*, *15*(2).

Rutgersson, A., Smedman, A., & Sahlée, E. (2011). Oceanic convective mixing and the impact on air-sea gas transfer velocity. *Geophysical Research Letters*, *38*(2).

Schuepp, P. H., Leclerc, M. Y., MacPherson, J. I., & Desjardins, R. L. (1990). Footprint prediction of scalar fluxes from analytical solutions of the diffusion equation. *Boundary-Layer Meteorology*, *50*(1-4), 355-373.

Schwartz, S. (1992). Factors governing dry deposition of gases to surface water. *Precipitation Scavenging and Atmosphere–Surface Exchange*, *2*, 789-801.

Seinfeld, J. H., & Pandis, S. N. (2016). *Atmospheric chemistry and physics: from air pollution to climate change*. John Wiley & Sons.

Silva, S. J., & Heald, C. L. (2018). Investigating Dry Deposition of Ozone to Vegetation. *Journal of Geophysical Research: Atmospheres*, *123*(1), 559-573.

Simpson, D., & Malik, S. (1996). Photochemical oxidant modelling and source-receptor relationships for ozone. *EMEP MSC-W Report*, *1*, 96.

Sorbjan, Z., & Grachev, A. A. (2010). An evaluation of the flux–gradient relationship in the stable boundary layer. *Boundary-layer meteorology*, *135*(3), 385-405.

Spence, C., Rouse, W. R., Worth, D., & Oswald, C. (2003). Energy budget processes of a small northern lake. *Journal of Hydrometeorology*, *4*(4), 694-701.
Stull, R. B. (2012). *An introduction to boundary layer meteorology* (Vol. 13). Springer Science & Business Media.

Sun, J., & Massman, W. (1999). Ozone transport during the California ozone deposition experiment. *Journal of Geophysical Research: Atmospheres*, *104*(D10), 11939-11948.

Suni, T., Berninger, F., Markkanen, T., Keronen, P., Rannik, Ü., & Vesala, T. (2003b). Interannual variability and timing of growing-season CO2 exchange in a boreal forest. *Journal of Geophysical Research: Atmospheres*, *108*(D9).

Suni, T., Rinne, J., Reissell, A., Altimir, N., Keronen, P., Rannik, U., Maso, M.D., Kulmala, M., & Vesala, T. (2003a). Long-term measurements of surface fluxes above a Scots pine forest in Hyytiala, southern Finland, 1996-2001. *Boreal Environment Research*, *8*(4), 287-302.

Sutton, O. G. (1953). *Micrometeorology: a study of physical processes in the lowest layers of the earth's atmosphere* (No. 551.50 SUT).

Vesala, T., Huotari, J., Rannik, Ü., Suni, T., Smolander, S., Sogachev, A., Launiainen, S., & Ojala, A. (2006). Eddy covariance measurements of carbon exchange and latent and sensible heat fluxes over a boreal lake for a full open-water period. *Journal of Geophysical Research: Atmospheres*, *111*(D11).

Vickers, D., & Mahrt, L. (1997). Quality control and flux sampling problems for tower and aircraft data. *Journal of Atmospheric and Oceanic Technology*, *14*(3), 512-526.

Vingarzan, R. (2004). A review of surface ozone background levels and trends. *Atmospheric Environment*, *38*(21), 3431-3442.

Wanninkhof, R., Asher, W. E., Ho, D. T., Sweeney, C., & McGillis, W. R. (2009). Advances in quantifying air-sea gas exchange and environmental forcing.

Wesely, M. L., Cook, D. R., & Williams, R. M. (1981). Field measurement of small ozone fluxes to snow, wet bare soil, and lake water. *Boundary-Layer Meteorology*, *20*(4), 459-471.

Wesely, M. L. (1989). Parameterization of surface resistances to gaseous dry deposition in regional-scale numerical models. *Atmospheric Environment (1967)*, *23*(6), 1293-1304.

Wesely, M. L., & Hicks, B. B. (2000). A review of the current status of knowledge on dry deposition. *Atmospheric environment*, *34*(12), 2261-2282.

Wetzel, R. G. (2001). *Limnology: lake and river ecosystems*. gulf professional publishing.

Wyngaard, J. C. (1990). Scalar fluxes in the planetary boundary layer—theory, modeling, and measurement. *Boundary-Layer Meteorology*, *50*(1-4), 49-75.

Young, P. J., Archibald, A. T., Bowman, K. W., Lamarque, J. F., Naik, V., Stevenson, D. S., Tilmes, S., Voulgarakis, A., Wild, O., Bergmann, D., & Cameron-Smith, P. (2013). Pre-industrial to end 21st century projections of tropospheric ozone from the

Atmospheric Chemistry and Climate Model Intercomparison Project (ACCMIP). *Atmospheric Chemistry and Physics*, *13*(4), 2063-2090.

Zhou, P., Ganzeveld, L., Rannik, Ü., Zhou, L., Gierens, R., Taipale, D., Mammarella, I., & Boy, M. (2017). Simulating ozone dry deposition at a boreal forest with a multi-layer canopy deposition model. *Atmospheric Chemistry and Physics*, *17*(2), 1361-1379.